JMEPEG (2026) 35:1886–1903
https://doi.org/10.1007/s11665-025-11639-y

©ASM International
1059-9495/$19.00

ORIGINAL RESEARCH ARTICLE

Influence of Ti on Structure, Tribology, and Corrosion of CoCrFeMnNiTi$_x$ High-Entropy Alloy

Caner Bulut, Fatih Yıldız, Temel Varol, Serhat Berk Akçay, and Tevfik Oğuzhan Ergüder

Submitted: 9 February 2025 / Revised: 29 April 2025 / Accepted: 22 May 2025 / Published online: 2 July 2025

In this study, high purity Co–Cr–Fe–Mn–Ni–Ti powders were produced by mechanical alloying, hot pressed at 650 MPa, and then sintered at 1000 °C for 2 h. The microstructural, mechanical, tribological, and corrosion properties of Ti-free (HEA-Ti$_0$-B), 3% Ti-added (HEA-Ti$_3$-B), and 5% Ti-added (HEA-Ti$_5$-B) high-entropy alloys (HEAs) were systematically investigated. The changes in the mass of the alloy powder materials were evaluated as a function of temperature and time using thermogravimetric analysis (TGA). At 850 °C, the HEA-Ti$_0$-P powders exhibited a mass gain of approximately 15.82%, while HEA-Ti$_3$-P and HEA-Ti$_5$-P showed increases of 26.83 and 28.55%, respectively. As confirmed by TGA, the increasing Ti content in the alloy powders led to a decrease in oxidation resistance. Microstructural analysis revealed that HEA-Ti$_0$-B exhibited a single-phase FCC structure, whereas Ti-containing alloys formed intermetallic phases. Porosity increased with Ti content, reaching 13.97% in HEA-Ti$_5$-B. Ti addition significantly enhanced mechanical performance, with HEA-Ti$_5$-B exhibiting the highest hardness (348.82 HB), a 32.2% improvement over HEA-Ti$_0$-B, alongside a 15.93% lower wear rate and 43.1% reduction in friction coefficient. However, in 3.5% NaCl medium, corrosion resistance decreased with increasing Ti addition and corrosion rates increased from 23.21 mpy (HEA-Ti$_0$-B) to 37.27 mpy (HEA-Ti$_5$-B). These findings highlight the trade-off between mechanical strength and electrochemical stability in Ti-containing HEAs.

Keywords CoCrFeMnNiTi$_x$, high-entropy alloys, microstructure, powder metallurgy, wear

1. Introduction

High-entropy alloys (HEAs) based on chemical disorder are one of the most innovative classes of materials and are of great interest to the scientific community due to their unusual properties (Ref 1). HEAs are complex alloys characterized by the presence of five or more principal elements, each in atomic concentrations ranging from approximately 5% to 35%, and often in nearly equal atomic percentages (Ref 2). HEAs offer a wide range of microstructures and properties depending on the alloying components and processing methods used. The superior properties of these alloys are due to factors such as high mixing entropy, lattice distortion, slow action and cocktail effect (Ref 3).

The CoCrFeMnNi structure, first reported by Cantor et al. (Ref 4), is among the most extensively studied HEA compositions in the literature. Although each element in this system has a different crystal structure, the alloy crystallizes as a single-phase face centered cubic (FCC) solid solution. The CoCrFeMnNi alloy system is known to exhibit a stable state, providing good combinations of strength and hardness, especially at cryogenic temperatures (Ref 5, 6). Nevertheless, this alloy demonstrates relatively low strength at ambient temperature. Thus, it has been reported to be inadequate for applications requiring high strength (Ref 7, 8). Improving the production properties and increasing the strength of this alloy is important to significantly increase its functionality in diverse applications. In this regard, various approaches, including work hardening, grain refinement, alloy hardening, precipitation hardening, and solid solution strengthening, are known to be employed to enhance the material's strength (Ref 9). Apart from these processes, compositional modification has also been the focus of studies to improve the properties of HEAs. Therefore, it is possible to improve the microstructure and properties by altering the composition and the content of certain elements in order to optimize the properties of the alloy for functional applications (Ref 10). It has been observed that the addition of low concentrations of titanium (Ti), niobium (Nb), or molybdenum (Mo) to this alloy system can lead to the formation of a hard secondary phase within the CoCrFeMnNi matrix, thereby improving its mechanical properties (Ref 11). Titanium and its alloys are preferred engineering materials because of their corrosion resistance, favorable biocompatibility, thermal stability, resistance to crack propagation, and high

Caner Bulut, Technical Sciences Vocational School, Iğdır University, 76000 Iğdır, Turkey; **Fatih Yıldız**, Department of Mechanical Engineering, Erzurum Technical University, 25100 Erzurum, Turkey; **Temel Varol**, Department of Metallurgical and Materials Engineering, Karadeniz Technical University, 61080 Trabzon, Turkey; Medical Device Design and Production Application and Research Center, Karadeniz Technical University, Trabzon, Turkey; and Advanced Engineering Materials Research Group, Karadeniz Technical University, Trabzon, Turkey; **Serhat Berk Akçay**, Department of Metallurgical and Materials Engineering, Karadeniz Technical University, 61080 Trabzon, Turkey; and and **Tevfik Oğuzhan Ergüder**, Department of Mechanical Engineering, Kafkas University, 36000 Kars, Turkey. Contact e-mails: caner.bulut86@erzurum.edu.tr and caner.bulut@igdir.edu.tr.

toughness at low temperatures. Additionally, the large atomic radius of Ti (1.47 Å) facilitates bonding with other elements in the CoCrFeMnNi alloy, which contributes to increased strength by influencing lattice distortion (Ref 12).

While HEAs can be produced through various methods, powder metallurgy (PM) stands out as a particularly effective technique. This method, which includes main processes such as mechanical alloying (MA), pressing and sintering, is notably efficient for enhancing the strength of the alloy (Ref 13). It is well known that MA produces a homogeneous microstructure and facilitates the formation of nanocrystalline grains. In contrast, synthesis using melting techniques can result in phase separation and inhomogeneous microstructures. In addition, MA is useful for synthesizing homogeneous alloys containing elements with different melting points and is also beneficial for alloys containing elements that do not mix in the liquid state (Ref 14). Joo et al. (Ref 15) produced CoCrFeMnNi HEA using MA and spark plasma sintering (SPS) and reported that the alloy retained its single-phase FCC structure up to 1100 °C and chromium carbides were formed due to milling-induced carbon, fine-grained microstructures with 60 min MA and 900 °C SPS, and bimodal microstructures after 60 min MA. Akhlaghi et al. (Ref 16) synthesized $CoCrFeMnNiTi_{0.1}$ alloys by MA and sintering methods and reported that milling for more time reduced grain size and improved mechanical properties. Cheng et al. (Ref 13) used powder metallurgy to incorporate Ti and C into the FeCoCrNiMn HEA. They observed that the alloy's microstructure consisted of an FCC solid solution matrix with minor amounts of TiC and other carbides. The addition of Ti and C improved the mechanical properties of the alloy, attributing these enhancements to grain boundary and precipitation strengthening mechanisms.

In our previous study (Ref 17), CoCrFeMnNi alloy powders were synthesized via MA with varying milling times, and samples were produced from these powders under different hot pressing pressures, followed by a sintering process. The structural and tribological properties of the resulting CoCrFeMnNi HEA samples were investigated. In the present study, in order to further improve the mechanical and tribological properties of the alloy, the production parameters of the sample that exhibited the best performance in the previous study were employed, and varying amounts of Ti were introduced into these samples. Accordingly, a comprehensive evaluation of the structural, mechanical, tribological, and corrosion behaviors of the newly developed HEA samples has been conducted. In the existing literature, the effects of Ti addition on various production methods have been investigated; however, studies focusing on the PM method remain limited, and a comprehensive evaluation of the structural, mechanical, tribological, and corrosion properties of CoCrFeMnNiTix HEAs has not yet been conducted. Therefore, in this study, the influence of Ti addition on the mechanical, tribological, and corrosion properties of CoCrFeMnNi HEAs produced via the PM method has been systematically investigated. To the best of the authors' knowledge, this research represents one of the first comprehensive assessments of the structural, mechanical, tribological, and corrosion behaviors of Ti-containing CoCrFeMnNi HEAs produced by powder metallurgy.

2. Experimental Details

2.1 Fabrication of $CoCrFeMnNiTi_x$ Powders

In this study, high-purity commercially available powders of Co-Cr-Fe-Mn-Ni-Ti (>99% purity) were used to produce CoCrFeMnNi HEA with compositions Ti-free (HEA-Ti_0-P), 3% Ti-added (HEA-Ti_3-P), and 5% Ti-added (HEA-Ti_5-P). The obtained powders were milled with no Ti and with varying amounts of Ti-added, and the MA process was carried out for 5 h. Detailed chemical composition of $CoCrFeMnNiTi_x$ powders is given Table 1. The parameters presented in Table 2 were implemented using a Retsch PM 100 planetary ball mill for the MA processes. WC jars and 10 mm-diameter balls were utilized as milling ambient. Methanol served as the process control agent (PCA) throughout all MA processes being added to the jar only at the outset of the procedure. A ball-to-powder ratio (BPR) of 10:1 was employed during all MA processes. The MA process was carried out using a program of 2 min milling followed by 1 min pause to avoid oxidation due to increased temperature with deformation in the milling jar.

2.2 Fabrication of $CoCrFeMnNiTi_x$ HEA Bulk Materials

After the MA process, the alloy powders were filled into molds with a diameter of 15 mm to fabricate $CoCrFeMnNiTi_x$ HEA compact materials, which were then densificated using the hot-pressing technique. The samples were coded as Ti-free (HEA-Ti_0-B), 3% Ti-added (HEA-Ti_3-B) and 5% Ti-added (HEA-Ti_5-B) according to their Ti content, and the production parameters are presented in Table 3. In the production of each sample, a hot-pressing duration of 2 h at 600 °C and a pressure of 650 MPa were used for the densification of HEA powders. To enhance the densification capability and reduce friction in the mold, graphite lubricant was used. Subsequently, all specimens were sintered in an argon atmosphere in a furnace at 1000 °C with a dwell time of 2 h. The sintering process was carried out by using 10 °C/min heating rate.

2.3 Characterization Studies of Powders and Samples

Particle size distribution was measured using the Malvern Mastersizer Hydro 2000. X-ray Diffraction (XRD) analysis of both powder and bulk samples was conducted with a GNR Explorer x-ray diffractometer, utilizing a Cu-Kα anode x-ray source with a wavelength of 1.5405 Å. Measurements were taken at 0.05° steps per second in a symmetrical scan mode within a range of 20° to 100°. For microstructural imaging and elemental analysis, scanning electron microscope (SEM) and energy dispersive spectrometry (EDS) were carried out with a Quanta-FEG 250 instrument. Thermogravimetric analysis was executed on a PerkinElmer TGA 4000 thermogravimetric analyzer, spanning a temperature range from 30 to 850 °C with a heating rate of 20 °C/min. The samples' surfaces were ground to 1200 grit and polished using alumina suspension. For microstructural examinations, the samples were chemically etched in a solution of HCl, HNO_3, and distilled water in a 1:1:1 ratio. Surface morphologies of the experimental samples were examined using a Carl Zeiss Scope A1 optical microscope (OM) and SEM, and cross-sectional images obtained from the optical microscope were analyzed with ZEISS ZEN 3.7 software to assess occupancy and relative density rates, followed by additional image analysis. Hardness tests were

Table 2 Parameter data of CoCrFeMnNiTi$_x$ powder

Code of powders	Milling speed, rpm	BPR	PCA, % wt.	Milling time, h
HEA-Ti$_0$-P HEA-Ti$_3$-P HEA-T$_5$-P	400	10:1	2	5

Table 3 Production process parameters of CoCrFeMnNiTi$_x$ HEA samples

Sample code	Milling time, h	Pressure, MPa	Hot-pressing temperature, °C	Hot-pressing time, h	Sintering temperature, °C	Sintering time, h
HEA-Ti$_0$-B HEA-Ti$_3$-B HEA-Ti$_5$-B	5	650	600	2	1000	2

*B Bulk.

conducted using a Brinell hardness testing machine, employing a 2.5 mm diameter steel ball and applying a load of 31.25 kgf.

2.4 Wear and Corrosion Tests

Surface roughness and wear volume of the samples were analyzed using the Bruker Contour GT 3D optical profilometer. The average roughness (Ra) values were determined by analyzing images from five different regions of each sample's surface. To investigate the effect of Ti addition on the wear resistance of CoCrFeMnNiTi$_x$ HEAs, tribological tests were performed with a Bruker-UMT tribometer with the parameters outlined in Table 4. Wear volumes were measured by the 3D profilometer by calculating the cross-sectional area of the wear tracks averaged from ten measurements multiplied by the length of each track using Vision64 software. Each sample was subjected to wear tests conducted three times, with detailed parameters provided in Table 4, and the wear rates were calculated using the formula presented below (Ref 18).

$$\text{Wear Rate}\left(\frac{\text{mm}^3}{\text{Nm}}\right) = \frac{\text{Wearvolume}(\text{mm}^3)}{\text{Wear distance (m)} \times \text{Normal load (N)}} \quad \text{(Eq 1)}$$

Corrosion tests were conducted at room temperature in a 3.5 wt% NaCl solution, with the corrosion resistance of all specimens assessed through potentiodynamic polarization. Prior to testing, the samples underwent metallographic polishing. Measurements were executed using a Gamry Series G750 potentiostat/galvanostat, and the resultant corrosion data were analyzed with Gamry Echem Analyst software. A standard three-electrode configuration was utilized at the electrochemical workstation, equipped with a corrosion cell to facilitate the generation of polarization curves. In this configuration, the Ag/AgCl electrode acted as the reference electrode (RE), the HEA corrosion samples functioned as the working electrode, and the graphite electrodes served as the counter electrode (CE). The surfaces of the test samples were insulated with tape, limiting the effective area to 1 cm^2. To achieve a steady-state potential, the open circuit potential (OCP) was recorded over a duration of 7200 s. Potentiodynamic polarization curves were obtained within a potential range of − 0.5 to + 2 V_{Ref} at a scan rate of 1 mV/s. Following the electrochemical assessments, the morphological characteristics of the corroded samples were examined using SEM.

Table 4 The parameters for the wear tests

Test parameters	Values
Test type	Reciprocating
Normal load, N	5
Velocity, mm/s	8
Ball type	Al_2O_3
Stroke, mm	4
Temperature, °C	Room temperature (23 ± 2)
Time, s	3600
Ambient	Dry conditions

3. Results and Discussion

3.1 Properties of CoCrFeMnNiTix HEA Powder Produced by MA

In our previous study (Ref 17), the effects of different milling durations (1, 3, and 5 h) and hot-pressing pressures on the microstructure, relative density, hardness, and wear resistance of CoCrFeMnNi HEA powders produced via MA were systematically investigated. The study revealed that while 1 h of milling produced fine powders, a more homogeneous and single-phase FCC structure began to form after 3 h, becoming dominant at 5 h. Additionally, longer milling durations led to enhanced cold welding and embedding of oxidation-resistant elements such as Co, Cr, and Ni into ductile Fe particles, thereby improving the oxidation resistance of the powders. Among the various conditions studied, powders milled for 5 h and hot-pressed at higher pressures exhibited the most homogeneous microstructure, the highest relative density, the greatest hardness and the lowest wear rate and friction coefficient. Accordingly, the milling time was determined as 5 h and different amounts of Ti were added to the alloy system to further enhance the performance of CoCrFeMnNi HEA in this

study. The morphological images and EDS analyses of HEA-Ti_0-P, HEA-Ti_3-P, and HEA-Ti_5-P HEA powder particles are presented in Fig. 1. According to the EDS results, the samples generally exhibit a homogeneous distribution. This finding indicates that the powder mixing and milling processes and milling times employed were successful. The ball milling process has a direct effect on particle morphology, resulting in the formation of a uniform particle with a single morphology due to the ball-powder-ball deformation at the end of the milling period. This result, repeated high-energy impacts between balls and powder particles provide sufficient plastic deformation and localized heating, facilitating the cold welding and fracture mechanisms specific to MA process (Ref 19).

Additionally, surface oxides can be detected in EDS analyses as shown in Fig.1. Although high purity elemental powders (>99%) were used, the presence of oxygen in the powders before sintering can be attributed to several factors. During MA, the repeated collisions between the balls and the powders produce significant local heating and plastic deformation, which can promote surface oxidation in the presence of residual oxygen in the milling medium. Furthermore, although methanol was used as the PCA and a 2 min milling/1 min pause cycle was applied to minimize oxidation due to temperature increase, exposure of the powders to ambient air (during powder preparation, loading or evaporation of PCA can lead to a certain level of oxygen adsorption or surface oxide formation. The high surface area of the fine powders in particular increases the susceptibility to surface oxidation.

Figure 2 shows the particle size distribution curves of HEA-Ti_0-P, HEA-Ti_3-P and HEA-Ti_5-P powders. The terms d(0.1), d(0.5), and d(0.9) obtained from particle size distribution analysis are used to indicate the particle size corresponding to a

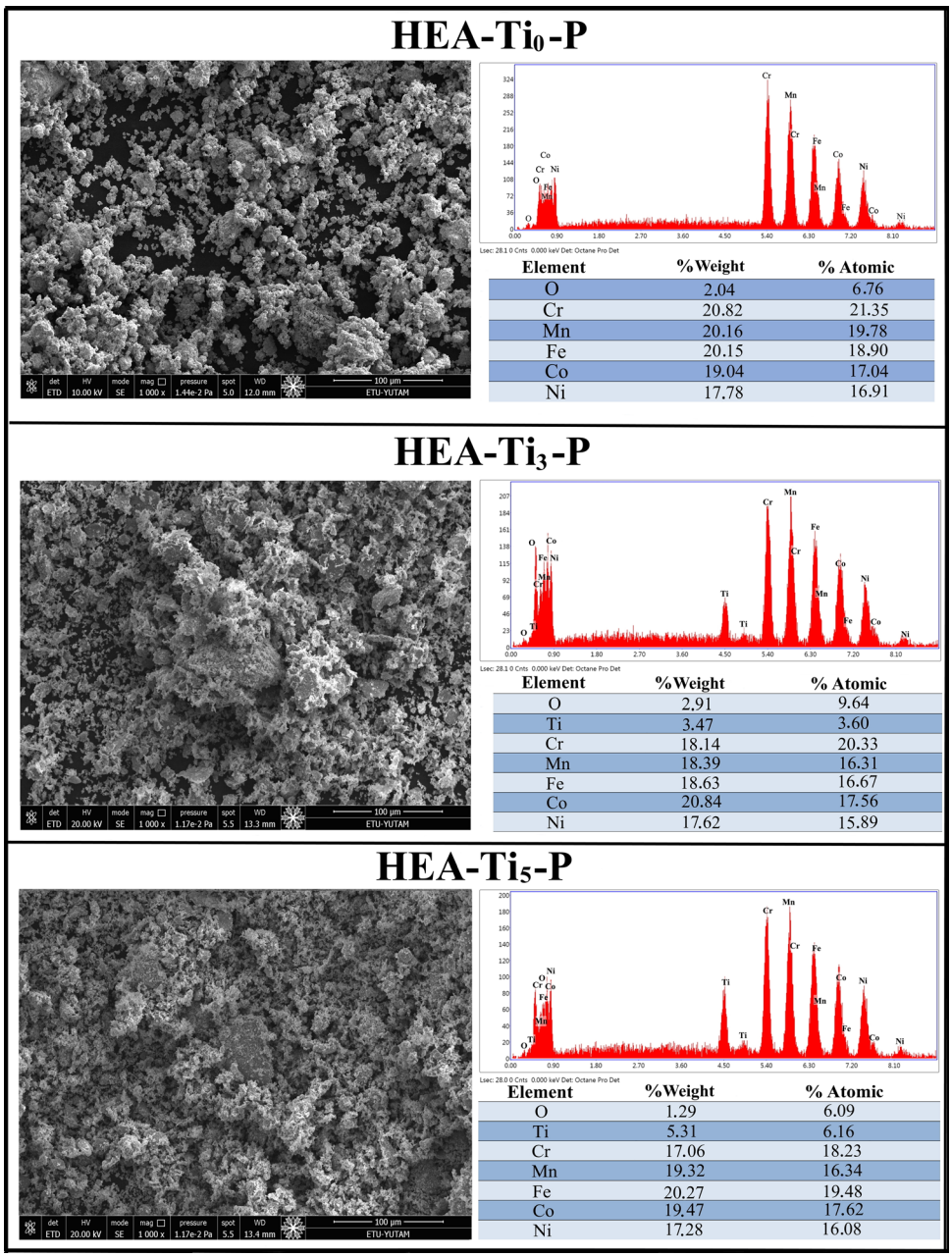

Fig. 1 SEM and EDS results of HEA-Ti_0-P, HEA-Ti_3-P, and HEA-Ti_5-P powders

certain portion of the powder within the bulk. In this context, the term d(0.1) means that 10% of the powder particles in the sample have a particle size smaller than the value defined by d(0.1). Similarly, d(0.5) indicates that 50% of the particles in the powder bulk have a size smaller than the value specified by d(0.5). Lastly, the term d(0.9) shows that 90% of the powder particles have a size smaller than the particle size value represented by d(0.9) (Ref 20). The particle size distribution of the powders HEA-Ti_0-P after 5 h of milling is between approximately 0.9 and 200 μm. However, a careful examination of the curve shows that the densest particle distribution by volume is approximately between 3 μm and 60 μm. The ball milling process has a significant effect on the particle size distribution of HEA powders. During the early stage of ball milling, the particles are rapidly reduced in size by fracture and shear forces, resulting in a broad distribution. Because, in the milling jar there are some deformations between ball to powder, powder to jar and powder to powder. As a result of these deformations particles deformed and particle size reduced because of the fracture. The particle size distribution of the HEA-Ti_3-P powder is significantly reduced compared to that of the HEA-Ti_0-P powder. The particle size distribution varies between 0.5 and 60 μm. However, it is predominantly seen that the powder volume is concentrated between 2 and 20 μm.

With the addition of Ti, the hardness of HEA particles increases, and they break into small pieces due to their brittleness as a result of deformations during the ball milling process. This leads to a narrowing of the particle size distribution and smaller particle sizes. There are also studies in the literature on the increase in hardness with Ti addition. Okumuş and Kaya carried out studies with 4% and 8% Ti doped HEA materials in their study. As a result of their study, they determined that 8% Ti doped materials have higher hardness than 4% Ti doped materials at different milling times (Ref 21). The particle size distribution curve of HEA-Ti_5-P powder shows a distribution range from 0.2 to 150 μm. However, the dominantly volume of the distribution was obtained between approximately 2 to 55 μm. These results are consistent with the $d_{(0.1)}$, $d_{(0.5)}$ and $d_{(0.9)}$ values obtained after particle size distribution tests as shown in Table 5. Zhao et al. reported that the particle size decreased as the Ti content increased in the W-TiC/Ti alloy using the mechanical milling method (Ref 22). Initially, the addition of low amounts of Ti increases the plastic deformation capability of the milling media, causing the particles to break more easily and thus reducing the particle size; however, as the Ti content increases, the deformation effect due to the reactive properties of titanium and its properties such as susceptibility to cold welding dominate the adhesion of the particles instead of breakage. This results in the deformation caused by the high energy in the milling vessel resulting in agglomeration rather than further fining of the particles. The high surface energy and low bulk deformation hardening tendency of titanium also favor this process, resulting in both an increase in average particle size and a wider size distribution.

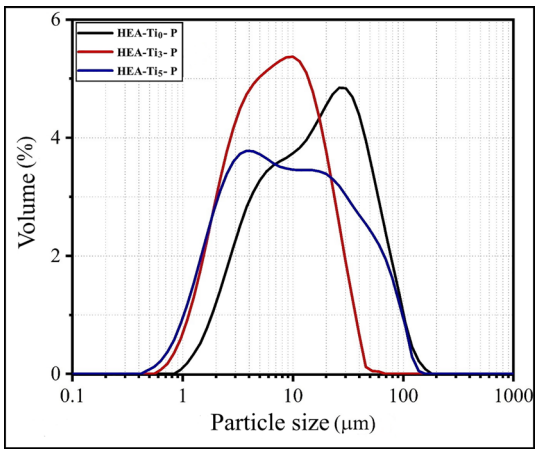

Fig. 2 Particle size distribution curves of the samples

The XRD patterns of HEA-Ti_0-P, HEA-Ti_3-P, and HEA-Ti_5-P powders subjected to MA treatment for 5 h are presented in Fig. 3. As explained in detail in our previous study (Ref 17), it was observed that the relative density of the FCC phase increased and the alloy powders predominantly formed the FCC primary phase after 5 h of milling. The HEA-Ti_3-P and HEA-Ti_5-P alloy powders exhibited a primary FCC phase structure, further crystallizing, and after a milling time of 5 h, Ti was homogeneously distributed within the alloy. In addition to the primary FCC phase in these alloy powders, several small peaks corresponding to Cr_7C_3(ICDD card number 00-006-0687, International Centre for Diffraction Data) are also observed. These peaks are believed to result from carbon contamination, which may originate from the graphite lubricant used in the dies, as well as from powder and WC balls present in the milling medium. The presence of broad XRD peaks resulting from milling time in all three alloys generally indicates the formation of nanocrystalline powders.

Thermogravimetric analysis (TGA) results from 30 to 850 °C of the samples are shown in Fig. 4. As seen in Fig. 4(a), the curve obtained as a result of 5 h milling of HEA-Ti_0-P powders shows a mass increase of approximately 15.82% when the temperature of 850 °C is reached. At 850 °C, the mass increases of HEA powders with HEA-Ti_3-P and HEA-Ti_5-P were 26.83% and 28.55%, respectively. It can be understood that the mass gain of HEA-Ti_5-P powders is approximately 80.46% higher than that of HEA-Ti_0-P powders and 6.41% higher than that of HEA-Ti_3-P powders. This result indicates a decrease in oxidation resistance as the Ti content in the structure increases. Qin et al. reported a decrease in oxidation resistance as the TiO formation increased in the CoCrCuFeNi-TiO alloy they produced (Ref 23). Figure 4(b) and 4(c) contains the temperature values at 5% and 10% mass increase, respectively. As can be seen in Fig. 4(b), the temperature values at which the mass increase is 5% for HEA-Ti_0-P, HEA-Ti_3-P, and HEA-Ti_5-P are 550 °C, 435 °C, and 405 °C, respectively. This means that HEA-Ti_5-P powders start to oxidize at lower temperature values compared to other powders. Similarly, in Fig. 3(c), the temperatures at which 10% mass increase is observed are 724, 520, and 480 °C for HEA-Ti_0-P, HEA-Ti_3-P, and HEA-Ti_5-P, respectively. These results show that the oxidation resistance of 5% Ti-added HEA-Ti_5-P powders is quite low compared to other powders. TGA

Table 5 Particle size distribution data for the powders

Sample powder code	$d_{(0.1)}$, μm	$d_{(0.5)}$, μm	$d_{(0.9)}$, μm
HEA-Ti_0-P	3.635	17.411	60.865
HEA-Ti_3-P	2.166	7.393	22.651
HEA-Ti_5-P	1.987	9.504	54.026

experiments conducted on powders of HEA-Ti_3-P and HEA-Ti_5-P have demonstrated a significant decrease in oxidation resistance with increasing Ti content. In other words, as the Ti content increased, the mass gain with increasing temperature also increased. This result shows that the higher Ti content promotes the formation of non-protective oxide layers within the structure due to Ti's affinity for oxygen. This phenomenon can be explained by the formation of TiO_2 oxides, which, as reported in the literature, react more readily with oxygen at high temperatures due to their low Gibbs free energy (Ref 24).

3.2 Properties of CoCrFeMnNiTix HEA Bulk Materials

3.2.1 Structural properties. Figure 5, 6 and 7 present the morphological images and EDS analysis results for HEA-Ti_0-B, HEA-Ti_3-B, and HEA-Ti_5-B samples. It is observed that all samples exhibit a homogeneous elemental distribution. Additionally, the Ti element is distributed very close to the targeted ratios in HEA-Ti_3-B and HEA-Ti_5-B samples. This result indicates that the milling time used was successful. It is well recognized that EDS provides only semi-quantitative results for light elements such as oxygen, particularly in surface-sensitive analyses (Fig. 1) of powder samples. The oxygen detected in the as-milled powders (HEA-Ti_0-P, Ti_3-P, Ti_5-P) is primarily considered to surface oxidation and possible moisture adsorption during powder handling and sample preparation. As illustrated in the SEM-EDS analyses of the sintered bulk samples (HEA-Ti_0-B, Ti_3-B, Ti_5-B), the oxygen content is significantly reduced to negligible levels, indicating that the vacuum sintering process at 1000 °C for 2 h effectively eliminated surface oxides formed during MA. This finding is further supported by the compact and homogeneous microstructures observed in the SEM images, with no evidence of oxide inclusions or secondary oxide phases in the bulk samples. Even under vacuum sintering conditions, residual surface oxidation may persist due to Ti segregation at particle boundaries or surfaces. Additionally, minor surface oxidation during post-sintering sample preparation for EDS analysis cannot be fully excluded. However, the microstructure of HEA-Ti_5-B appears to remain dense and uniform, suggesting that the observed presence of oxygen may not have a significant adverse effect on the structural integrity or expected performance of the sintered HEA samples.

XRD graphs of HEA-Ti_0-B, HEA-Ti_3-B, and HEA-Ti_5-B alloy samples are presented in Fig. 8. The HEA-Ti_0-B sample exhibits a single FCC main phase structure. An increase in peak intensity was observed after sintering, which can be attributed to both the partial elimination of residual stresses induced during MA and the grain growth resulting from thermal activation at elevated temperatures. The reason for the higher XRD peaks of bulk materials compared to powdered samples can also be explained by the fact that powders produced by mechanical milling have high internal stresses due to the deformation they are exposed to during the milling process. In other words, powders produced by milling are subjected to severe plastic deformation, leading to internal stress accumulation. However, during the bulk production process, the application of elevated temperatures helps to relieve these stresses, resulting in a more stable and stress-free structure. Consequently, problems such as low peak intensity caused by internal stresses are mitigated. Moreover, powdered samples generally have lower density and higher surface area compared to bulk materials, which can negatively affect x-ray scattering,

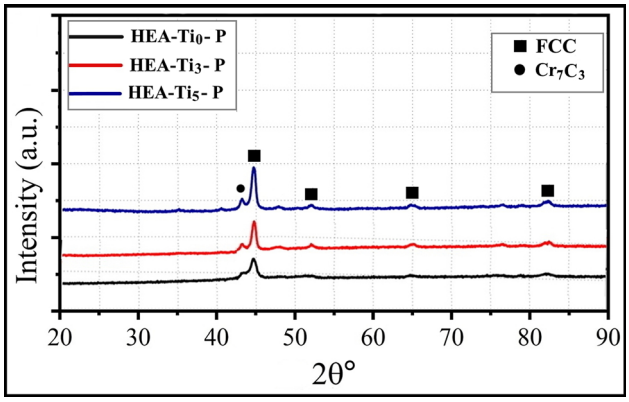

Fig. 3 XRD graphical of HEA-Ti_0-P, HEA-Ti_3-P and HEA-Ti_5-P powders

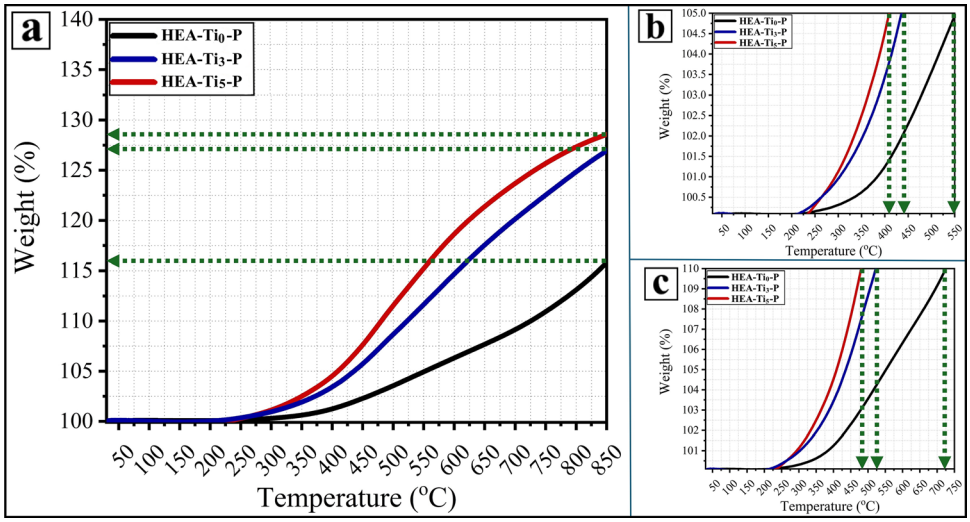

Fig. 4 TGA curves of the samples; (a) TGA graph from 30 °C to 850 °C, (b) TGA graph 5% weight loss and (c) TGA graph 10% weight loss.

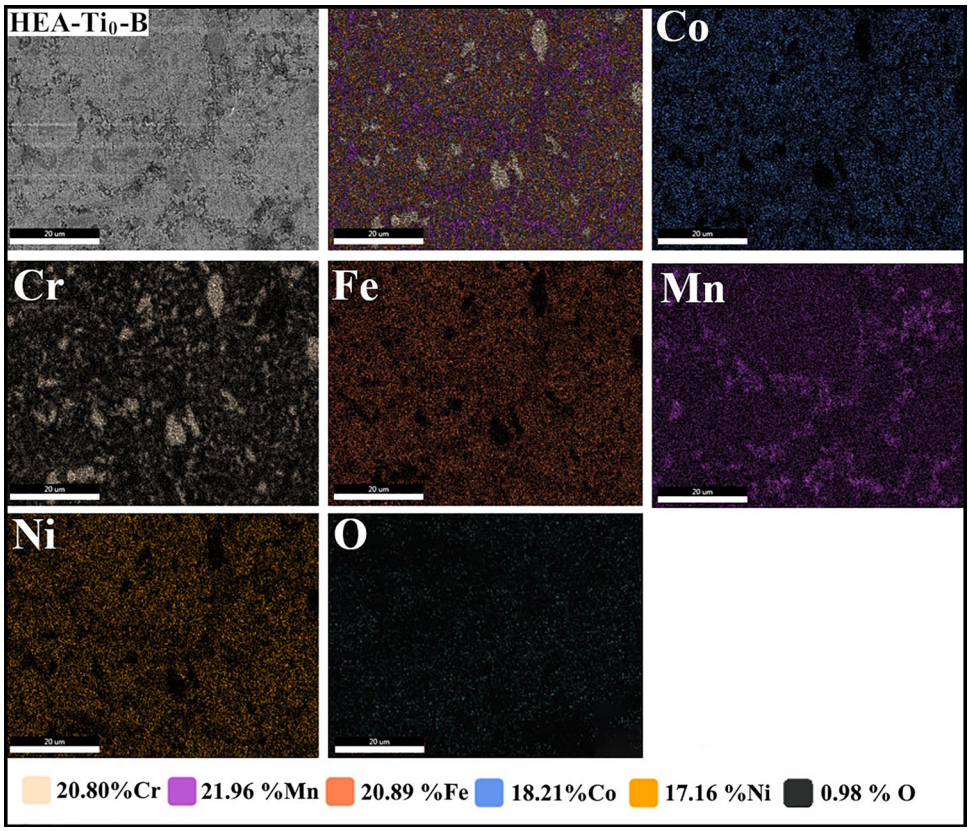

Fig. 5 SEM images and EDS analysis results of HEA-Ti_0-B sample

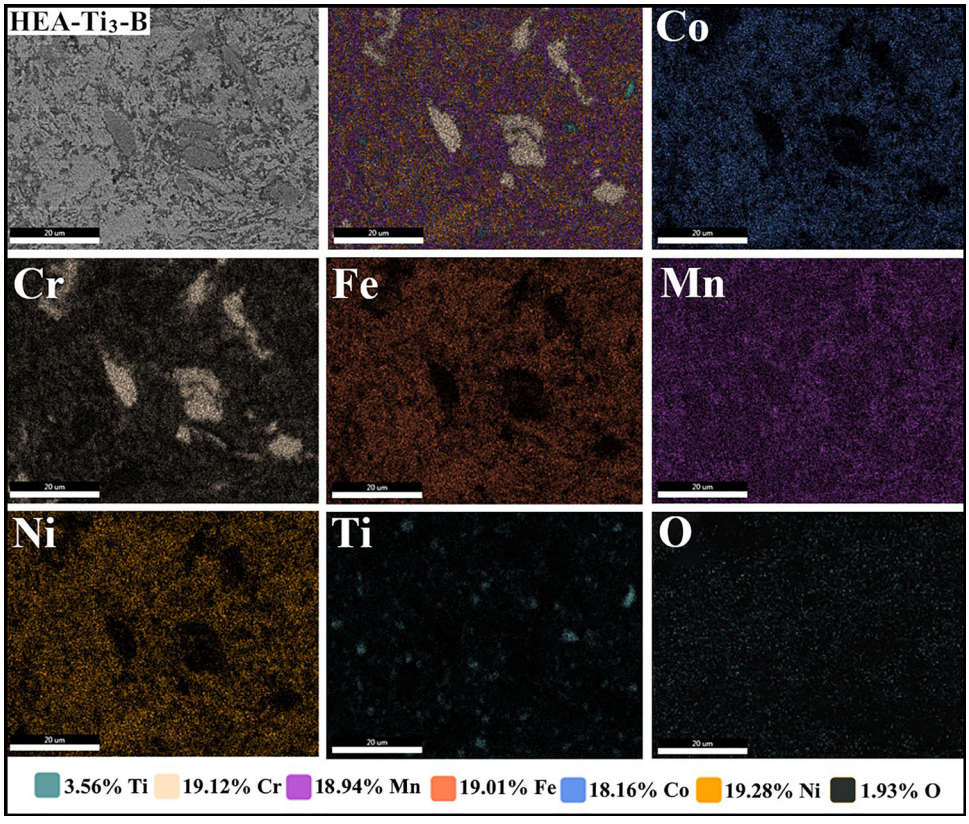

Fig. 6 SEM images and EDS analysis results of HEA-Ti_3-B sample

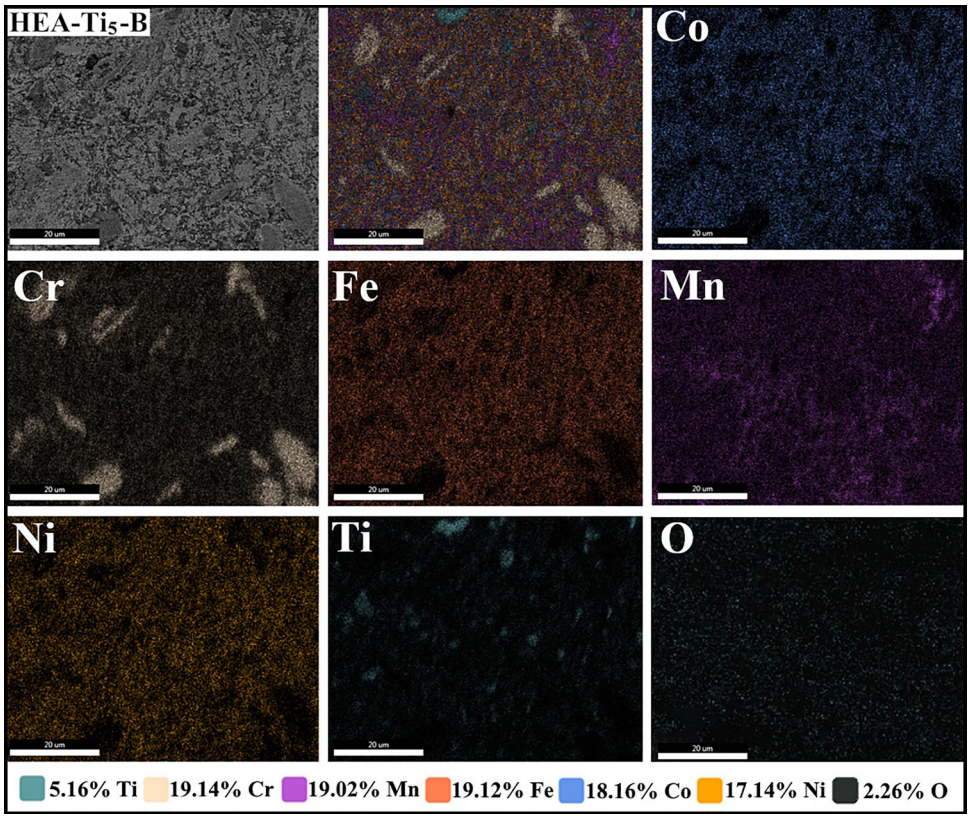

Fig. 7 SEM images and EDS analysis results of HEA-Ti_5-B sample

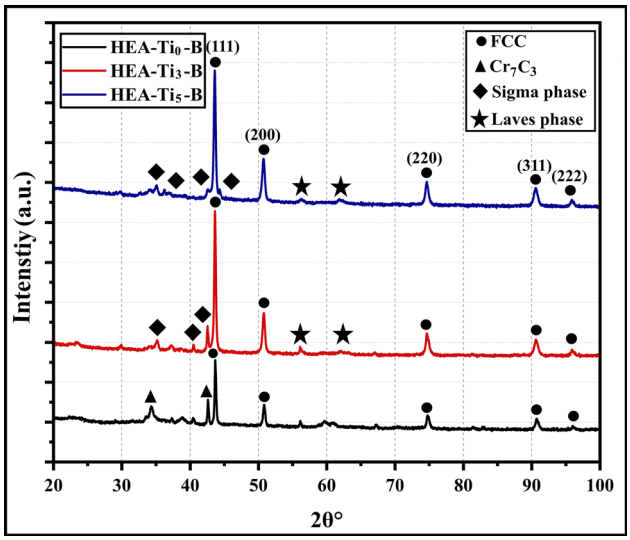

Fig. 8 XRD results of HEA-Ti_0-B, HEA-Ti_3-B, and HEA-Ti_5-B HEAs.

leading to reduced peak intensities. In contrast, bulk materials offer a more concentrated and homogeneously diffracting structure, contributing to higher peak intensities. Additionally, the temperature and pressure applied during the hot pressing and sintering process promote atomic diffusion and facilitate the rearrangement of the crystal structure. This not only enhances crystallinity but also helps eliminate defects and residual stresses, ultimately resulting in a significant increase in XRD peak intensities.

Additionally, very small amounts of Cr_7C_3 were formed during sintering in this sample (Ref 17). The development of the Cr_7C_3 phase is quite prevalent in CoCrFeMnNi alloys after sintering and heat treatment (Ref 25, 26). Here, C contamination is thought to originate from graphite lubricant used to reduce friction on the inner walls of the mold during hot pressing, contamination from powder, and milling WC balls. A minor shift in the FCC peaks can be detected as the addition of Ti increases. This shift occurs due to Ti's larger atomic diameter relative to other alloying elements (Ref 27). In addition to the main FCC phase structure in HEA-Ti_3-B and HEA-Ti_5-B samples, there are also weak reflection peaks associated with the sigma (σ) and Laves phases, which are recognized as intermetallic phases. Along with the increased addition of Ti, the density of these intermetallics in the HEA-Ti_5-B sample also rose. The presence of titanium significantly affects the transition from the FCC phase to the intermetallic phase structure in alloys (Ref 28). The addition of more Ti indicates a higher probability of the formation of intermetallic phases in the structures (Ref 29). This facilitates the formation of ordered intermetallic compounds such as Laves and σ phases due to Ti's relatively large atomic radius and strong negative enthalpy of mixing with elements such as Cr, Fe and Co, taking into account the contributions of both enthalpy and entropy to phase stability. Although HEAs are typically stabilized by their high configurational entropy, the strong enthalpic interactions introduced by Ti can override the entropy term in the Gibbs free energy equation ($\Delta G = \Delta H - T\Delta S$), favoring intermetallic phase formation. Where ΔH and ΔS are the enthalpy and entropy of hydride formation and T is the temperature. As shown by Yamanaka et al. (Ref 30), Ti addition in

CoCrFeMnNi-based systems notably stabilizes σ, A12, and C14-Laves phases, particularly when Cr is present. Therefore, the increased formation of intermetallic phases with higher Ti content is not only an experimental observation but also aligns well with thermodynamic expectations in multi-component alloy systems. It led to the formation of Fe-Cr type and Cr-Ti rich sigma phase and Co-Ti type laves phase in HEA-Ti_3-B and HEA-Ti_5-B samples. The density of these intermetallics in the samples has increased with higher Ti content, and numerous studies in the literature have reported the formation of intermetallic phases beyond the FCC peaks (Ref 16, 31, 32). These results obtained in Fig. 8 are consistent with the literature.

OM images of the samples and the results of relative density measurements obtained through image analysis are presented in Fig. 9. Sample relative densities were measured as 86.29% for HEA-Ti_0-B, 86.16% for HEA-Ti_3-B and 86.03% for HEA-Ti_5-B, respectively. According to the results, both milling time and the sintering process significantly influenced the relative densities, resulting in samples with a relative density exceeding 86% and maintaining volumetric integrity across all three samples. As Ti content increases from HEA-Ti_0-B to HEA-Ti_5-B, the relative density slightly decreases, which is evident in the micrographs as an increase in porosity and less compact grain boundaries. Especially in image HEA-Ti_5-B, a visibly more porous structure can be observed compared to HEA-Ti_0-B, supporting the measured relative density values.

SEM images of the microstructure taken from the etched samples are presented in Fig. 10. In the figure, all sample surfaces have light and dark gray grains and a dense microstructure. In these Ti-added samples (HEA-Ti_3-B and HEA-Ti_5-B) a more pronounced appearance is observed and the dark gray phases present tend to be homogeneously distributed throughout the matrix in fine grains interspersed with each other. The samples may contain Cr-enriched particles, sigma phase, and carbides. Due to the high affinity between elemental carbon and chromium during milling, the milled powders inevitably become contaminated with carbon from the PCA (Ref 16). Cr-rich zones begin to form during the initial stages of powder synthesis, and the resulting phase formation is influenced by the quantity of Cr deposited. If the amount of Cr in these regions is high, Cr_7C_3 is formed; if it is low, the sigma phase develops (Ref 33). The emergence of the sigma phase in Cr-rich areas is a result of the rapid diffusion of Cr at intermediate temperatures. The studies have shown that Cr plays a significant role in phase formation, directly influencing the phase microstructure, diffusion coefficients, and reactions between elements (Ref 34).

In general, when the crystal structures of the alloys are analyzed together with the XRD results, they agree with the findings reported by Cui et al. (Ref 35) and show that the increase in Ti content leads to the formation of intermetallic phases along with the FCC primary phase. Tsun et al. (Ref 36) reported that the microstructure consists of plate-like structures with a mixture of light and dark phases, along with abundant intermetallic phases such as Laves, R, and sigma phases, which are enriched with increasing Ti content. The applied hot pressing and sintering processes can influence the size distribution of these various phases in the microstructure. This is attributed to the increased diffusion rate at the sintering temperature (Ref 37). However, it is evident that the sintering process positively affects the sample densities. It was observed that the distance between the lamellae and grains decreased after sintering in the HEA-Ti_3-B and HEA-Ti_5-B samples, leading to the formation of more lamellar structures compared to the HEA-Ti_0-B sample. The lamellar structures observed in the HEA-Ti_3-B and HEA-Ti_5-B samples are believed to result from the addition of Ti. In addition, despite the hot pressing and sintering processes, the microstructure of the samples exhibits pores on the surfaces, characterized by voids and pores that indicate insufficient densification and interaction between the particles. The presence of voids and pores is influenced by both the powder morphology and the grinding time and pressing pressure applied. Çelebi et al. (Ref 38) stated that the powders behaved as if cold-pressed with minimal diffusion and solubility, leading to a porous and poorly sintered structure. They highlighted the necessity for higher processing temperatures or alternative mechanisms to improve diffusion and attain a denser microstructure. They reported that the presence of pores at grain boundaries reduces material homogeneity and negatively affects its performance. Sinha and Farhat (Ref 39) reported that the amount of lubricant used in the PM fabrication and sintering processes plays an important role in determining pore size, shape, and quantity. A slight increase in the amount of porosity is observed due to the increase in the Ti addition rate. Ti addition disrupted the lattice structure in HEA-Ti_3-B and especially HEA-Ti_5-B samples, leading to the formation of micro-voids in the regions where the grains meet/at grain boundaries.

3.2.2 Tribological Properties. The coefficient of friction (COF) findings for the HEA-Ti_0-B, HEA-Ti_3-B, and HEA-Ti_5-B samples produced with PM are presented in Fig. 11. The surface roughness of the samples was measured immediately after production and the values recorded were 4.12 μm for the HEA-Ti_0-B sample, 4.70 μm for the HEA-Ti_3-B sample and

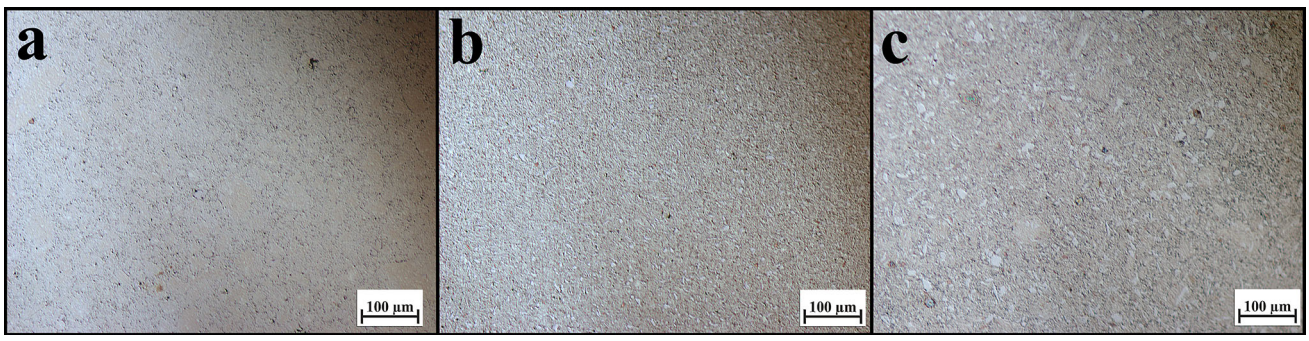

Fig. 9 OM images of the (a) HEA-Ti_0-B, (b) HEA-Ti_3-B, and (c) HEA-Ti_5-B samples

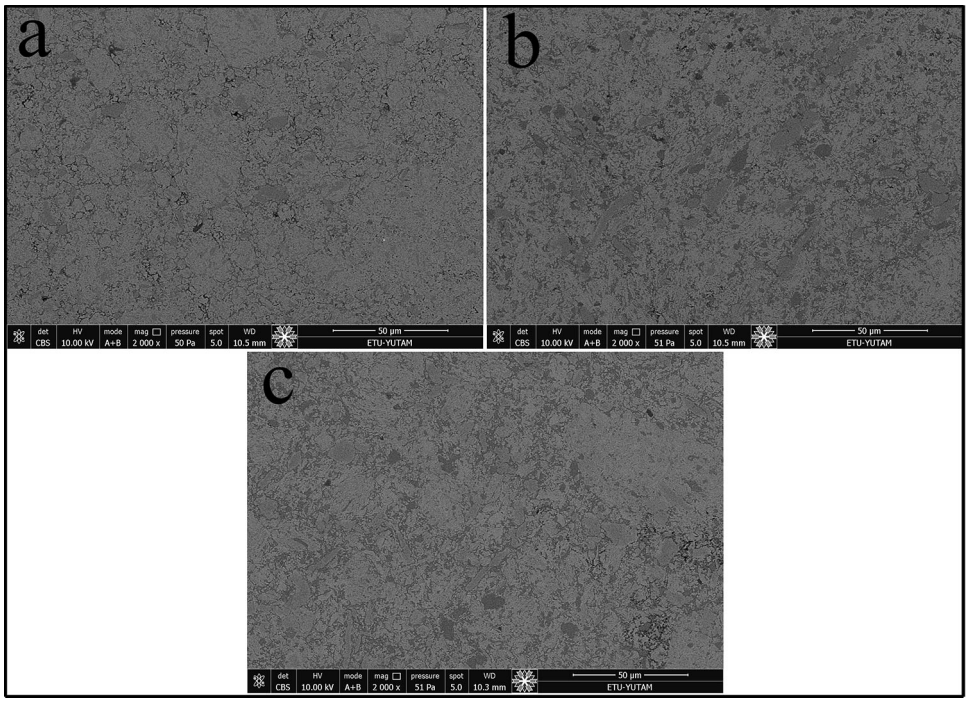

Fig.10 SEM images of the microstructure of the samples: (a) HEA-Ti_0-B, (b) HEA-Ti_3-B, (c) HEA-Ti_5-B.

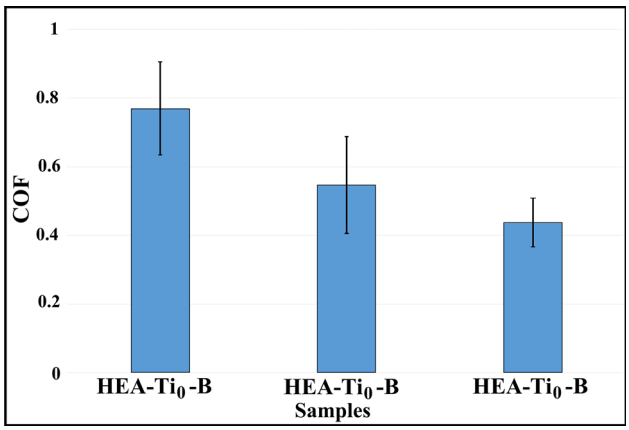

Fig. 11 COF-time plot of HEA-Ti_0-B, HEA-Ti_3-B, and HEA-Ti_5-B samples

4.32 μm for the HEA-Ti_5-B sample. Before the wear test, the surface roughness of all samples was prepared to an average value of 0.05 μm through metallographic processes.

The COF values of the specimens initially rose with the first contact at the start of the wear test, eventually stabilizing as the surfaces and the counter abrasive (Al_2O_3 ball) adapted to one another. There is an observed decrease in the COF values of the specimens in parallel to the increasing Ti content. The HEA-Ti_3-B sample exhibited an increasing trend at the end of the initial period and started to flatten toward the end of the test. The HEA-Ti_5-B specimen exhibits a more stable form from the beginning of the test to the end of the test period. In general, slight fluctuations in COF were detected for all samples, and this can be attributed to the plastic deformation during the contact of friction pairs and the presence of wear products formed during the test. Table 6 shows the wear test results and

Table 6 Tribological and hardness values for HEA-Ti_0-B, HEA-Ti_3-B, and HEA-Ti_5-B

Sample code	COF	Hardness, HB	Wear rate, mm^3/Nm
HEA-Ti_0-B	0.7699	263.8	2.24733×10^{-5}
HEA-Ti_3-B	0.5468	300.36	2.12836×10^{-5}
HEA-Ti_5-B	0.4380	348.82	1.88916×10^{-5}

hardness measurements of the samples. The average COF value of the HEA-Ti_5-B sample is about 43.1% lower than that of the HEA-Ti_0-B sample and about 19.9% lower than that of the HEA-Ti_3-B sample. Wang et al. (Ref 40) stated that the development of an oxide film effectively separates the metal surfaces under normal loads, decreasing metallic contact between the sliding surfaces and consequently resulting in a lower COF. Yu et al. (Ref 41) reported COF values for CrC-reinforced CoCrFeMnNi HEAs to be around 0.5 to 0.8. Nagarjuna et al. (Ref 42) reported that the increasing HfO_2 content in the CoCrFeMnNi alloy produced by PM led to a decrease in the average COF values.

In Fig. 12, the wear rate and hardness values of HEA-Ti_0-B, HEA-Ti_3-B, and HEA-Ti_5-B samples are presented on graph. There is a tendency for a decrease in wear rates and a significant increase in hardness with increasing Ti content. HEA-Ti_5-B specimen exhibits a higher hardness value and lower wear rate behavior compared to other specimens. The HEA-Ti_0-B specimen has a hardness of 263.8 HB and the highest wear rate. The average hardness values of the HEA-Ti_3-B and HEA-Ti_5-B samples were 300.36 HB and 348.82 HB, respectively. These results indicate that, in terms of hardness values with Ti addition in the samples, the HEA-Ti_3-B sample exhibited an improvement of approximately 13.9%, whereas

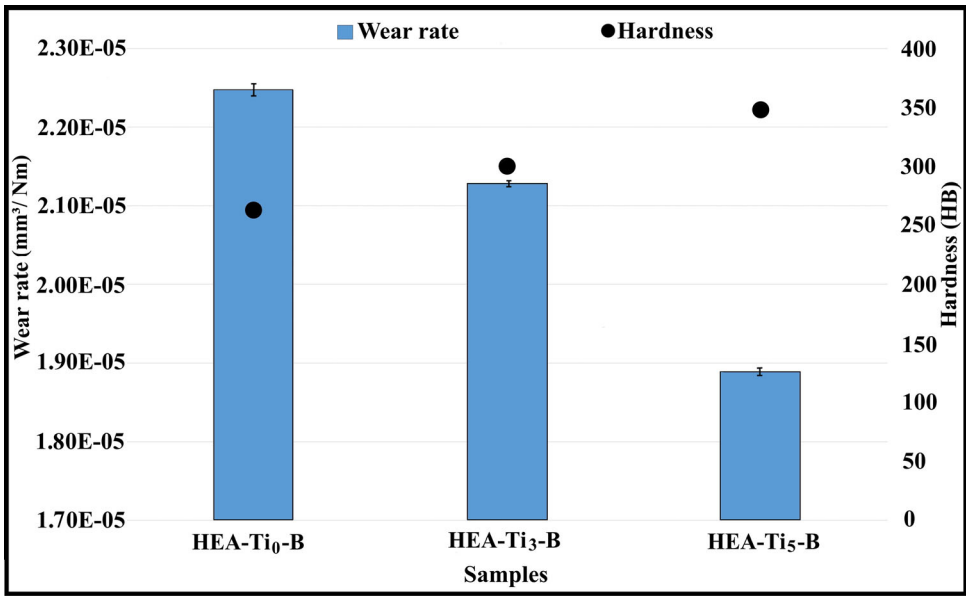

Fig. 12 Wear rate and hardness values for HEA-Ti_0-B, HEA-Ti_3-B, and HEA-Ti_5-B

the HEA-Ti_5-B sample showed an improvement of about 32.2% compared to the HEA-Ti_0-B sample. The increase in hardness observed in the HEA-Ti_3-B and HEA-Ti_5-B specimens can be associated with lattice distortion resulting from the addition of Ti to the alloy as well as the presence of hard intermetallic phases (Ref 43). Nam et al. (Ref 44) reported that the increasing Ti content and the presence of intermetallic phases in the alloy structure produced using the PM method with different Ti additions led to an increase in strength and hardness values, ultimately improving the mechanical properties.

SEM and optical profilometer images of wear tracks of HEA-Ti_0-B, HEA-Ti_3-B, and HEA-Ti_5-B samples are given in Fig. 13, 14, and 15, respectively. When the wear track widths are examined in the figures, the wear track width (Fig. 15b, c) of the HEA-Ti_5-B sample, which has the highest surface hardness and the lowest wear rate value, is lower than the wear track widths of the other samples (HEA-Ti_0-B and HEA-Ti_3-B). The HEA-Ti_3-B sample also demonstrated superior wear performance in comparison with the HEA-Ti_0-B sample, exhibiting a reduction in track formation and both lower wear volume and wear rate values (Fig. 14b, c). The HEA-Ti_5-B sample exhibits a wear rate approximately 15.93% lower than the HEA-Ti_0-B sample, while the HEA-Ti_3-B sample exhibits a wear rate approximately 5.29% lower than the HEA-Ti_0-B sample. The HEA-Ti_5-B sample resulted in a lower contact area of the counterpart material. Therefore, as the frictional contact area remained low, the adhesive wear mechanism became more passive, and the HEA-Ti_5-B specimen wore less than the other specimens. In our previous study, compared to the CoCrFeMnNiTi_x (x = 0, 3, and 5) HEA alloy produced by selective laser melting (SLM) with the same composition, the samples produced by powder metallurgy in this study exhibited significantly better wear performance than those produced by SLM (Ref 10). In all three samples, the wear mechanism appears to be a dominant combination of adhesive wear, abrasive wear, and plastic deformation mechanisms. As a result, it was found that the addition of Ti to CoCrFeMnNi HEA significantly improved the hardness value and wear rate.

During the wear test, the sample surfaces are exposed to scratches due to the reciprocating movements of the Al_2O_3, and the HEA samples undergo plastic deformation. As the test progresses and the sliding distance increases, the contact pressure diminishes at both the micro- and macro-levels. This leads to a larger contact area. While the reduction in contact pressure results in lower wear severity, the increased contact area causes the wear track to grow larger (Ref 45). This situation became more evident, especially on the HEA-Ti_0-B sample surface (Fig. 13a, b, c). On the wear surfaces of this sample, when the degree of plastic deformation exceeds a certain threshold, under the influence of wear mechanisms, the formation of metallic plate-like wear residues/layers and large flake-shaped wear debris indicating adhesive wear begins, starting from the surface (Fig. 13b-c'). As the test progresses, various delaminations/local cracks are observed on the worn surface, and it is seen that severe plastic deformation occurs as shown in Fig. 13b, c, c'. Delaminations and plastic flow in the worn surface layers are attributed to the ductile properties of FCC structures, which are mainly characterized by their low hardness (Ref 46).The cross-sectional microstructure of the wear track for this sample (Fig. 13c') confirmed the delamination of large flake-shaped wear deposits, along with layers and boundary cracks on the sample surfaces after testing. In the advanced stages of testing, a large number of oxides accumulate to form a continuous oxide layer, which acts as a lubricant in the medium and protects the material surface from direct metal-metal bonding, consequently reducing wear rates. Wang et al. (Ref 47) reported that the oxide layer developed on the worn surface of the CoCrFeMnNi alloy is essential for lubrication, leading to a reduction in both the friction coefficient and wear rate under applied load. Nagarjuna et al. (Ref 48) reported that CoCrFeMnNi HEAs produced by the PM method at different milling times showed delamination and oxidation of wear debris in the worn surface layers, with the dominant wear being adhesive wear. As a result, the wear mechanism for the HEA-Ti_0-B sample is a combination of adhesive wear, with delamination and plastic deformation mechanisms being much more dominant. Liu et al. (Ref 49)

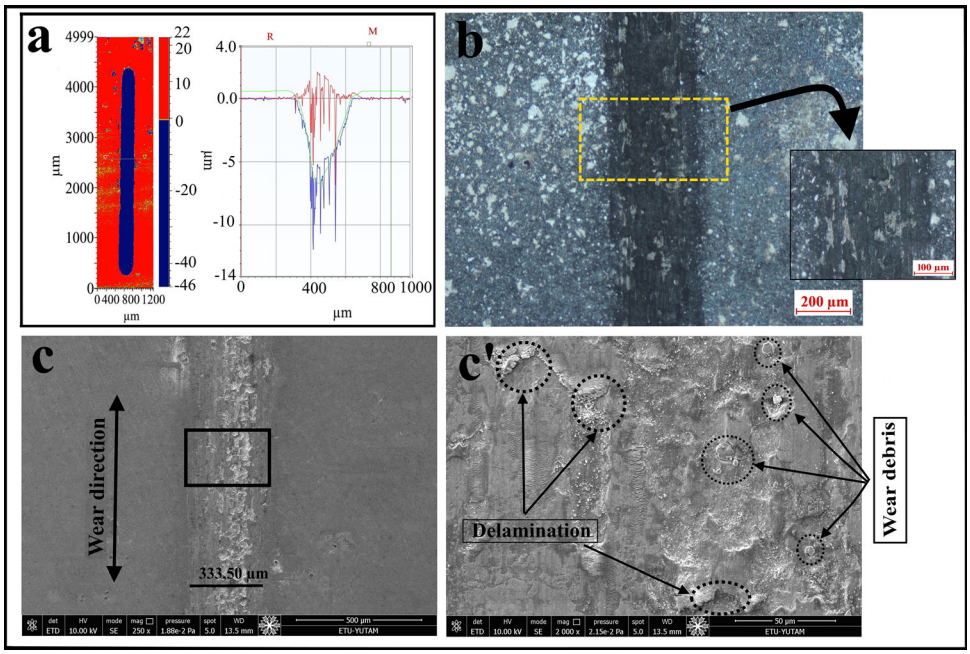

Fig. 13 HEA-Ti_0-B sample; (a, b) wear track 3D profilometer and OM images, (c, c′) SEM images of wear track

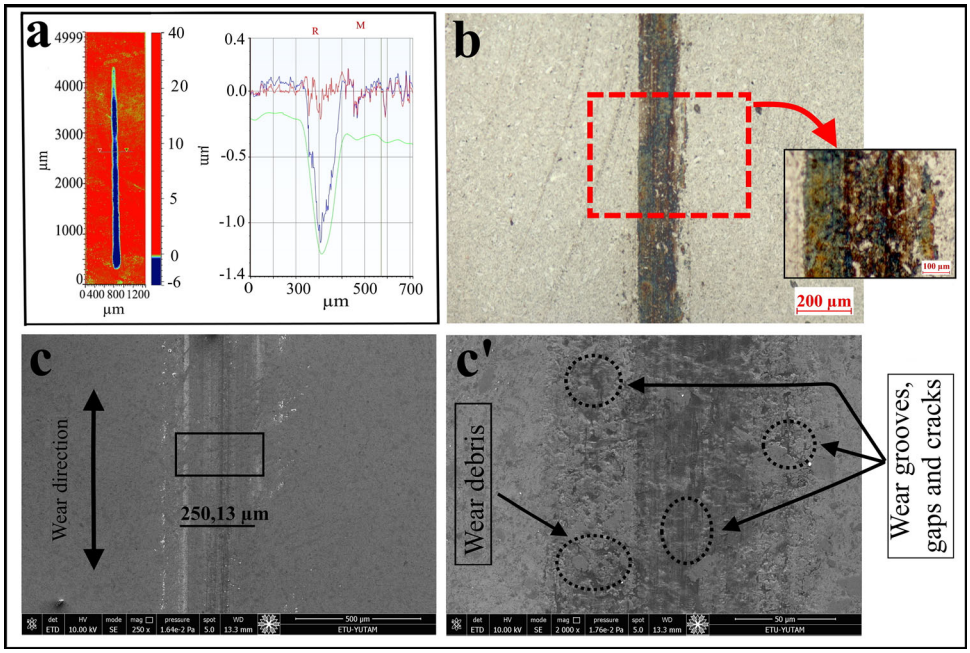

Fig. 14 HEA-Ti_3-B sample; (a, b) wear track 3D profilometer and OM images, (c, c') wear track SEM images

reported that samples fabricated with PM showed numerous deformations, grooves, and flaking features on the surfaces at the end of the wear test, and oxides were formed, indicating dominant adhesion wear and slight oxidation wear characteristics.

It was found that with increasing hardness, the effect of adhesive wear decreased and abrasive wear became more dominant in the HEA-Ti_3-B and HEA-Ti_5-B samples. This phenomenon was particularly pronounced in the HEA-Ti_5-B sample. The presence of pits, deep grooves, and scratches on the worn surfaces and in areas where wear debris was separated along the sliding direction of the HEA-Ti_3-B sample indicates that plastic deformation occurred in conjunction with wear debris. This finding suggests that the predominant wear mechanism was abrasive wear (Fig. 14). This is attributed to the entrapment of wear debris and particles on the worn surface during testing, which can lead to significant material wear (Ref 50). Therefore, it is observed that the wear mechanism in this sample is characterized by predominantly abrasive wear, combined with low levels of adhesive wear and plastic deformation (Fig. 14b-c'). Liu et al. (Ref 51) reported that the wear resistance of $CoCrFeMnNiTi_x$ coatings increased with increasing Ti content. They also reported that the wear surfaces of the samples displayed grooves, adhesions, cracks, chips, and

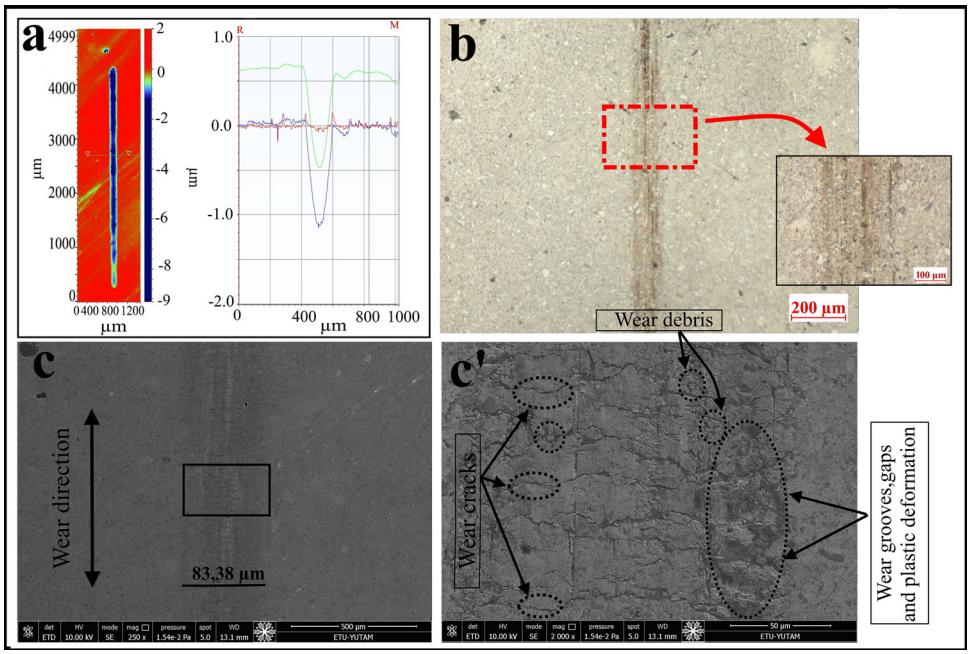

Fig. 15 HEA-Ti_5-B specimen; (a, b) wear track 3D profilometer and OM images, (c, c') SEM images of the wear track

small holes, indicating the presence of abrasive particles, characteristic of a typical abrasive wear mechanism. Test results stated that at room temperature, the wear mechanism of $CoCrFeMnNiTi_x$ HEA coatings was primarily abrasive wear, with adhesive wear and fatigue wear mechanisms also present. Wang et al. (Ref 52) reported that increasing Ti content led to improved wear resistance of $CoCrFeMnNiTi_x$ coatings, and the dominant wear mechanism was abrasive wear and oxidation wear.

The wear surface of the HEA-Ti_5-B sample exhibited an impression partially similar to the wear surface of the HEA-Ti_3-B sample (Fig. 15b, c). The worn surface of the HEA-Ti_5-B sample has developed pits, a dense formation of microcracks, and plastic deformation. However, oxidation formation and delamination damage on the worn surfaces of the HEA-Ti_5-B sample are not very dominant and are almost not observed. This indicates that delamination wear is minimized, and the morphology aligns with the observed low wear rate. The reduction in surface damage can be attributed to the effectiveness of the Ti addition, which increases hardness and prevents severe plastic deformation, as well as to the precipitation or presence of intermetallic phases in the FCC matrix. These brittle hard phases acted as a barrier against delamination wear (Ref 53). Lee et al. (Ref 54) stated that the delamination damage on the build surface of $FeCoNiAlSi_{0.2}$ HEA is less than that of the FeCoNiAl/WC pair, which leads to lower wear loss for $FeCoNiAlSi_{0.2}$ HEA. The wear surface of the specimen exhibits considerable roughness, featuring shallow grooves and surface cracks (Fig. 15c, c'). This indicates that both abrasive wear and plastic deformation contribute to surface damage. Overall, the wear rates of HEA specimens have a significant impact on the wear rates of the sample contents, particularly regarding the influence of Ti addition and intermetallic phases on wear resistance properties. Considering the surfaces where wear tests were conducted for all samples, it is observed that the HEA-Ti_5-B specimen exhibits superior performance in terms of wear resistance.

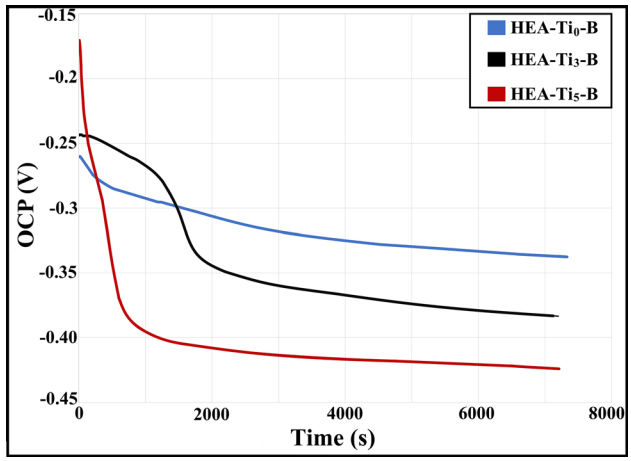

Fig. 16 OCP curves of HEA-Ti_0-B, HEA-Ti_3-B, and HEA-Ti_5-B

3.2.3 Corrosion Behaviors. OCP is a method used to study the behavior of a material during the corrosion process. Prior to the corrosion tests, the samples were prepared through metallographic processes, cleaned with ethyl alcohol, and then dried. The OCP curves for the HEA-Ti_0-B, HEA-Ti_3-B, and HEA-Ti_5-B samples are presented in Fig. 16. The OCP curves for all three samples gradually shift toward the cathodic direction or more negative (less noble) potential values during the testing period in the 3.5% NaCl solution. The potential stabilizes at approximately − 0.33 V against the graphite electrode for the HEA-Ti_0-B sample after 7200 s, at approximately − 0.38 V for the HEA-Ti_3-B sample, and at approximately − 0.43 V for the HEA-Ti_5-B sample. This situation indicates that passive layers have not formed on the samples or that they are very weak (Ref 55). In addition, the highest open circuit potential was obtained in the HEA-Ti_0-B sample, and therefore it can be said that this sample is the noblest. The most

active potential value belongs to the HEA-Ti_5-B sample. Therefore, a downward trend in OCP curves generally indicates that corrosion resistance has decreased or that the material's sensitivity to corrosive environments has increased and it may have begun to show less resistance. This situation can be attributed to a number of factors, including changes in the chemical composition of the samples, the presence of potential cracks on the surfaces, the porosity rate resulting from the manufacturing method, and the heterogeneity introduced by the intermetallic phases, particularly in the Ti-added samples. Öztürk et al. (Ref 56) stated that increasing the Ti content causes segregation in the microstructure of $CoCuFeMnNiTi_x$ alloys and that the amount of interdendritic regions in the microstructure increases with higher Ti content. They noted that this situation leads to phase separation and the formation of galvanic corrosion, ultimately reporting that increasing the Ti content in $CoCuFeMnNiTi_x$ alloys reduces corrosion resistance. Ren et al. (Ref 57) reported that high-density micropores cause extensive metastable pitting and that micro-segregation zones act as active sites for corrosion initiation.

Based on electrochemical corrosion theory, corrosion potential (E_{corr}) is considered a thermodynamic parameter, whereas corrosion current density (I_{corr}) is defined as a kinetic parameter (Ref 58). The corrosion potential indicates the electrochemical potential of a material in an open-circuit condition, while the corrosion current density can be utilized to assess the corrosion rate of metals. As the corrosion current density decreases, the corrosion rate also decreases, resulting in increased corrosion resistance. The potential at the bottom of the curves represents the corrosion potential, which reflects the stability of the system (Ref 55, 59).

HEA-Ti_0-B, HEA-Ti_3-B, and HEA-Ti_5-B samples' potentiodynamic polarization curves are presented in Fig. 17, and the data obtained from these curves are summarized in Table 7. Upon examining the potentiodynamic polarization curves in Fig. 17, it is observed that all three samples exhibit typical active-passive potential behavior in the 3.5 wt% NaCl solution. These results show that all three samples have corrosion resistance in chloride ambient. The HEA-Ti_0-B sample has the best corrosion properties, with higher E_{corr} (− 386.0 mV) and lower I_{corr} (57.7 x 10-6) values. An increase in corrosion rates was observed for the Ti-added HEA-Ti_3-B and HEA-Ti_5-B samples, parallel to the E_{corr} and I_{corr} results. For the HEA-Ti_0-B sample, the corrosion rate value is approximately 23.21 mpy, the corrosion rate of the HEA-Ti_3-B sample is approximately 27.81 mpy, and the corrosion rate of the HEA-Ti_5-B sample is approximately 37.27 mpy. One of the main factors affecting the corrosion rate is the corrosion current density (Ref 58, 60). It was observed that the I_{corr} values in the samples increased with higher Ti content. The HEA-Ti_5-B sample, with a corrosion potential of approximately − 0.49 V, was the first to undergo corrosion, and the highest corrosion current density was detected in this sample, making it the one with the highest corrosion rate. The higher corrosion rates of the other two samples compared to the HEA-Ti_0-B sample are attributed to their greater porosity, which is associated with the increased Ti content. This condition is one of the factors influencing corrosion rate efficiency. Furthermore, the intermetallic phases present in Ti-added specimens can disrupt the homogeneity of the metal structure (Ref 10). These phases have the potential to reduce the passivation tendency on the surfaces by consuming Cr, particularly in the HEA-Ti_3-B and HEA-Ti_5-B samples. This may be cited as a reason for the low corrosion resistance observed in the alloys. Liu et al. (Ref 61) reported that in the CoCrFeMnNiTix alloy they studied with laser cladding, increasing the Ti content (especially when Ti% exceeds 1.0) negatively affects corrosion behavior. They noted that this situation leads to the consumption of a certain amount of Cr by the laves phases in the structure, reducing the tendency for the Cr passive film to form and consequently increasing the corrosion rate.

Figure 18 shows SEM images of the surfaces of all three specimens following the corrosion tests. Intense corrosion damage, manifesting as pitting corrosion, has been observed on the surface of the HEA-Ti_0-B sample. Flaking/incrustation and cracking corrosion occurring on the sample surface before the formation of pits were detected. There are also oxide film fractures around the pits on the sample surface. It is possible to make a similar interpretation for the surface images of HEA-Ti_3-B and HEA-Ti_5-B samples. The extent of corrosion damage in these samples is even more pronounced. The depth of pits and voids increases with increasing Ti content. Compared to the other samples, it can be seen that the damage in the HEA-Ti_5-B sample penetrates deeper into the surface and the corrosion damage is more evident in the form of cracking and flaking.

Pure Ti is generally considered a passive metal in most aqueous environments, as it naturally forms a protective TiO_2-based film on its surface. The incorporation of Ti into HEAs is anticipated to influence corrosion resistance, particularly when Ti becomes part of the surface film. However, in multicomponent alloys, Ti often tends to react with other elements to form intermetallic compounds (Ref 62, 63). It has been reported in the literature that the presence of Ti favors the formation of laves phases of the Fe_2Ti and Co_2Ti type and of sigma phases of the R and FeCr type in HEA systems. (Ref 64, 65). It can be inferred from the existing literature that the microstructure of many Ti-containing HEAs can become more heterogeneous due to the formation of such bonding metallic compounds, which have relevant implications for corrosion resistance. The formation of these compounds generally results in an overall reduction in corrosion of multi-component alloys, particularly when Ti is present (Ref 56). In this context, the different distribution of σ and laves phases in the HEA-Ti_3-B and HEA-Ti_5-B samples, along with the differing electrode potentials of these phases, led to the formation of microcellular voids in the structure, further increasing the corrosion rate. Moreover, the formation of intermetallic phases within the structure can result in a certain amount of Cr consumption, thereby reducing the passivation tendency of Cr in the sample. These intermetallic phases therefore increase the susceptibility to local attack, and their dissolution during cyclic potentiodynamic polarization testing results in corrosion of the material (Ref 61, 66). As a result, although the passivation zone expanded with increasing Ti content, the insufficient protective capacity of the formed layer led to a reduction in the corrosion resistance of the alloys. Consequently, the corrosion resistance decreased in correlation with the rising Ti content.

4. Conclusions

In this study, HEA-Ti_0-B, HEA-Ti_3-B and HEA-Ti_5-B samples were successfully fabricated using the PM method. The effects of Ti addition on the microstructure, mechanical properties, tribological behavior, and corrosion resistance of the

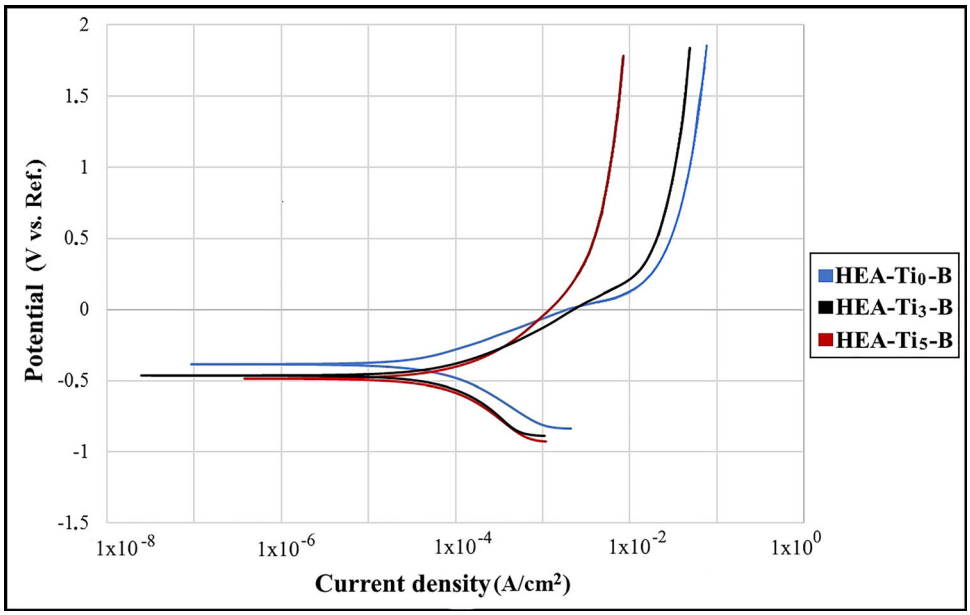

Fig. 17 Polarization curves of HEA-Ti_0-B, HEA-Ti_3-B, and HEA-Ti_5-B samples

Table 7 Results of the potentiodynamic polarization tests for the HEA-Ti_0-B, HEA-Ti_3-B, and HEA-Ti_5-B samples

Sample Code	E_{corr}, mV	I_{corr}, A/cm^2	Corrosion rate , mpy
HEA-Ti_0-B	−386.0 ± 2	57.7 x 10^{-6} ± 3 x 10^{-6}	23.21
HEA-Ti_3-B	−462.0 ± 5	69.1 x 10^{-6} ± 9 x 10^{-6}	27.81
HEA-Ti_5-B	−484.0 ± 2	92.6 x 10^{-6} ± 12 x 10^{-6}	37.27

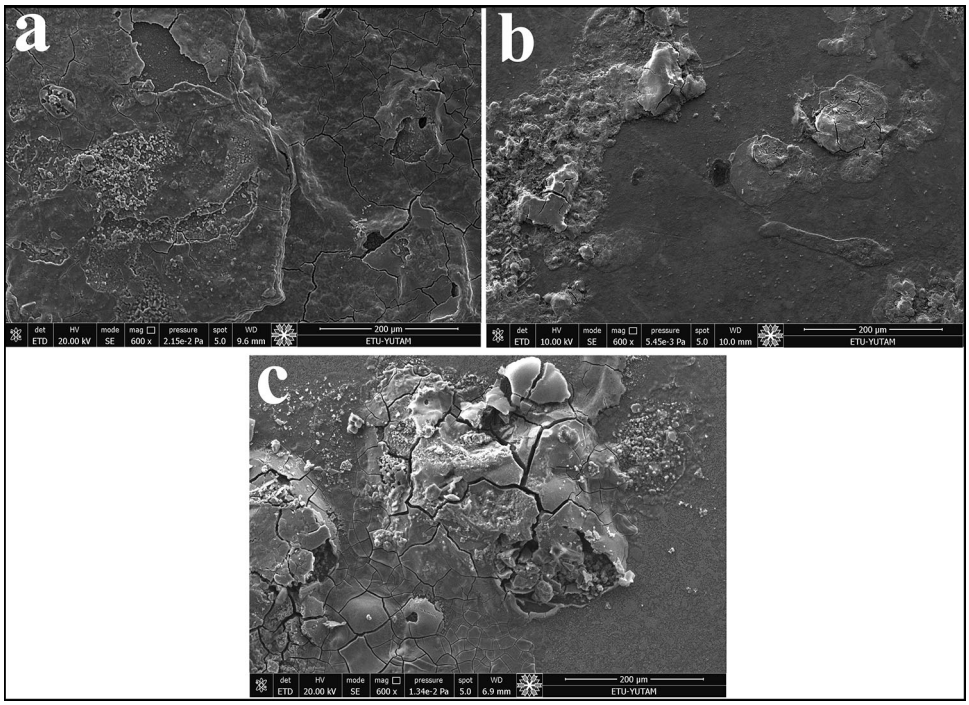

Fig. 18 SEM surface images of corrosion test of PM samples; (a) HEA-Ti_0-B, (b) HEA-Ti_3-B, (c) HEA-Ti_5-B

alloys were systematically investigated. The key findings are summarized below:

- According to the EDS results, the Co-Cr-Fe-Mn-Ni-Ti elements exhibited a generally homogeneous distribution in both the alloy powders obtained through mechanical alloying and in all produced samples.
- The HEA-Ti_0-P alloy powder exhibited the densest particle distribution in the range of approximately 3 to 60 μm. In contrast, the Ti-added alloy powders had smaller particle sizes compared to the HEA-Ti_0-P alloy powder, with HEA-Ti_3-P concentrating in the range of 2 to 20 μm and HEA-Ti_5-P in the range of 2 to 55 μm.
- When the temperature of 850 °C was reached, the HEA-Ti_0-P powders had a mass increase of approximately 15.82%, while the mass increases of HEA powders containing HEA-Ti_3-P and HEA-Ti_5-P were 26.83 and 28.55%, respectively. A decrease in oxidation resistance was observed in the samples with increasing Ti addition.
- According to the XRD results, the HEA-Ti_0-B sample exhibited a dominant FCC primary phase along with weak Cr_7C_3 formation attributed to the production process. With increasing Ti addition, a dominant FCC main phase along with intermetallic phases with weak reflection peaks corresponding to σ and laves phases were observed in HEA-Ti_3-B and HEA-Ti_5-B samples.
- All sample groups had relative density exceeding 86%; however, the increase in Ti content in the HEA-Ti_3-B and HEA-Ti_5-B samples resulted in a slight increase in porosity. The HEA-Ti_5-B sample exhibited the highest porosity at 13.97%, while the HEA-Ti_0-B sample showed the lowest porosity at 13.71%. All samples were observed to be homogeneously distributed throughout the matrix in a fine-grained and lamellar form.
- With the addition of Ti and the effect of the intermetallic phases in these samples, the hardness values of the HEA-Ti_3-B and HEA-Ti_5-B samples increased. The HEA-Ti_5-B sample had a higher hardness value of 348.82 HB compared to the other samples, which showed an improvement of approximately 32.2% compared to the HEA-Ti_0-B sample.
- With the increase in Ti ratio, the wear resistance of the samples improved and COF values decreased. The average COF value of the HEA-Ti_5-B sample was approximately 43.1% lower than that of the HEA-Ti_0-B sample and about 19.9% lower than that of the HEA-Ti_3-B sample. Additionally, the HEA-Ti_5-B sample exhibited a wear rate approximately 15.93% lower than that of the HEA-Ti_0-B sample, while the HEA-Ti_3-B sample showed a wear rate approximately 5.29% lower than that of the HEA-Ti_0-B sample.
- The HEA-Ti_0-B sample exhibited the best corrosion properties with a higher E_{corr} (− 386.0 mV) and lower I_{corr} (57.7×10^{-6}). The corrosion rate for the HEA-Ti_0-B sample was approximately 23.21 mpy, while the HEA-Ti_3-B and HEA-Ti_5-B samples had corrosion rates of approximately 27.81 mpy and 37.27 mpy, respectively. As a result, the corrosion resistance decreased with increasing Ti content.

Acknowledgments

This study is supported by the Scientific and Technological Research Council of Türkiye (TÜBİTAK) with the project code 122M679. We would like to thank TÜBİTAK for its contributions.

Author's Contribution

CB: Investigation, Writing—review and editing, Validation. FY: Conceptualization, Writing—review and editing, Supervision. TV: Investigation, Writing—review and editing, Validation. SBA: Investigation, Writing—review and editing, Validation. TOE: Investigation, Writing—review and editing, Validation.

Data Availability

The data supporting the findings of this study are available within the article.

Conflict of interest

All authors declare that there are no competing interests. The authors have no competing interests to declare that are relevant to the content of this article.

Ethical Approval

Not applicable.

References

1. Y. Zhang, T.T. Zuo, Z. Tang, M.C. Gao, K.A. Dahmen, P.K. Liaw, and Z.P. Lu, Microstructures and Properties of High-Entropy Alloys, *Prog. Mater. Sci.*, Elsevier Ltd, 2014, **61** p 1–93, https://doi.org/10.1016/j.pmatsci.2013.10.001
2. C. Bulut, Y. Fatih, T. Varol, G. Kaya, and T.O. Ergüder, Effects of Selective Laser Melting Process Parameters on Structural, Mechanical, Tribological and Corrosion Properties of CoCrFeMnNi High Entropy Alloy, *Met. Mater. Int.*, The Korean Institute of Metals and Materials, 2024, (0123456789), https://doi.org/10.1007/s12540-024-01694-w
3. J.W. Yeh, Alloy Design Strategies and Future Trends in High-Entropy Alloys, *Jom*, 2013, **65**(12), p 1759–1771
4. B. Cantor, I.T.H. Chang, P. Knight, and A.J.B. Vincent, Microstructural Development in Equiatomic Multicomponent Alloys, *Mater. Sci. Eng. A*, Elsevier, 2004, **375**–**377**(1-2 SPEC. ISS.), p 213–218, https://doi.org/10.1016/j.msea.2003.10.257
5. E.S. Kim, K.R. Ramkumar, G.M. Karthik, S.G. Jeong, S.Y. Ahn, P. Sathiyamoorthi, H. Park, Y.U. Heo, and H.S. Kim, Cryogenic Tensile Behavior of Laser Additive Manufactured CoCrFeMnNi High Entropy Alloys, *J. Alloys Compd.*, Elsevier, 2023, **942**, p 169062, https://doi.org/10.1016/j.jallcom.2023.169062
6. Y.K. Kim, M.C. Kim, and K.A. Lee, 1.45 GPa Ultrastrong Cryogenic Strength with Superior Impact Toughness in the in-Situ Nano Oxide Reinforced CrMnFeCoNi High-Entropy Alloy Matrix Nanocomposite Manufactured by Laser Powder Bed Fusion, *J. Mater. Sci. Technol.*, Elsevier Ltd, 2022, **97**, p 10–19, https://doi.org/10.1016/j.jmst.2021.04.030
7. F. Otto, Y. Yang, H. Bei, and E.P. George, Relative Effects of Enthalpy and Entropy on the Phase Stability of Equiatomic High-Entropy Alloys, *Acta Mater.*, 2013, **61**(7), p 2628–2638. https://doi.org/10.1016/j.actamat.2013.01.042
8. X. Wang, Q. Liu, Y. Huang, L. Xie, Q. Xu and T. Zhao, Effect of Ti Content on the Microstructure and Corrosion Resistance of CoCrFeNiTix High Entropy Alloys Prepared by Laser Cladding, *Materials (Basel)*, 2020, **13**(10), p 1–13
9. M. Naghizadeh and H. Mirzadeh, Microstructural Evolutions During Annealing of Plastically Deformed AISI 304 Austenitic Stainless Steel: Martensite Reversion, Grain Refinement, Recrystallization, and Grain

Growth, *Metall. Mater. Trans. A Phys. Metall. Mater. Sci.*, Springer US, 2016, **47**(8), p 4210–4216, https://doi.org/10.1007/s11661-016-3589-1
10. C. Bulut, F. Yıldız, T. Varol and T.O. Ergüder, Effect of Titanium on the Structural, Mechanical and Surface Properties of CoCrFeMnNiTix High Entropy Alloy Fabricated by Selective Laser Melting, *Intermetallics*, 2024, **169**, p 15. https://doi.org/10.1016/j.intermet.2024.108281
11. F. He, Z. Wang, J. Wang, Q. Wu, D. Chen, B. Han, J. Li, J. Wang, and J.J. Kai, Abnormal Γ″ - ε Phase Transformation in the CoCrFeNiNb0.25 High Entropy Alloy, *Scr. Mater.*, Acta Materialia Inc., 2018, **146**, p 281–285, https://doi.org/10.1016/j.scriptamat.2017.12.009
12. D. Yang, Y. Liu, H. Jiang, M. Liao, N. Qu, T. Han, Z. Lai, and J. Zhu, A Novel FeCrNiAlTi-Based High Entropy Alloy Strengthened by Refined Grains, *J. Alloys Compd.*, Elsevier B.V, 2020, **823**
13. H. Cheng, W. Chen, X. Liu, Q. Tang, Y. Xie, and P. Dai, Effect of Ti and C Additions on the Microstructure and Mechanical Properties of the FeCoCrNiMn High-Entropy Alloy, *Mater. Sci. Eng. A*, Elsevier B.V., 2018, **719,** p 192–198, https://doi.org/10.1016/j.msea.2018.02.040
14. R.K. Mishra and R.R. Shahi, Novel Co 35 Cr 5 Fe 20 Ni 20 Ti 20 High Entropy Alloy for High Magnetization and Low Coercivity, *J. Magn. Magn. Mater.*, 2019, **484**, p 83–87
15. S.H. Joo, H. Kato, M.J. Jang, J. Moon, E.B. Kim, S.J. Hong, and H.S. Kim, Structure and Properties of Ultrafine-Grained CoCrFeMnNi High-Entropy Alloys Produced by Mechanical Alloying and Spark Plasma Sintering, *J. Alloys Compd.*, Elsevier B.V, 2017, **698**, p 591–604, https://doi.org/10.1016/j.jallcom.2016.12.010
16. P. Akhlaghi, M. Amirjan, and N. Parvin, The Effect of Processing Parameters and Heat-Treatment on the Microstructure and Mechanical Properties of PM CoCrFeMnNiTi$_{0.1}$ High-Entropy Alloy, *Mater. Chem. Phys.*, Elsevier B.V., 2021, **257**, p 123722, https://doi.org/10.1016/j.matchemphys.2020.123722
17. C. Bulut, F. Yıldız, T. Varol, S.B. Akçay and T.O. Ergüder, The Effect of Milling Time and Hot-Pressing on the Structural Properties and Wear Behavior of CoCrFeMnNi High-Entropy Alloys Fabricated by Mechanical Alloying, *High Temp. Corros. Mater.*, 2024, **101**(2), p 225–249. https://doi.org/10.1007/s11085-023-10213-y
18. H.C. Aksa, İ. Hacısalihoğlu, F. Yıldız, T. Varol, O. Güler, G. Kaya, and S.B. Akçay, Effects of Fabrication Parameters and Post-Processing Treatments on the Mechanical and Tribological Behavior of Surface-Enhanced Copper Based Materials by Selective Laser Melting, *J. Mater. Process. Technol.*, 2022, **304**, https://doi.org/10.1016/j.jmatprotec.2022.117564
19. C. Suryanarayana, Mechanical Alloying and Milling, *Prog. Mater. Sci.*, 2001, **46**(1–2), p 184, https://doi.org/10.1016/S0079-6425(99)00010-9
20. O. Çuvalcı, T. Varol, S.B. Akçay, O. Güler, and A. Çanakçı, Effect of Ball Mill Time and Wet Pre-Milling on the Fabrication of Ti Powders by Recycling Ti Machining Chips by Planetary Milling, *Powder Technol.*, 2023, **426**, https://doi.org/10.1016/j.powtec.2023.118637
21. M. Okumuş and F. Kaya, Effect of Ti Content and Ball-Milling Time on the Microstructural, Thermal, and Microhardness Properties of AlCoCuNiTi High Entropy Alloys, *Mater. Chem. Phys.*, 2024, **311**
22. S. Zhao, Y. Lv, Z. Zhang, T. Liu, and J. Fan, Materials Science & Engineering A The Microstructure and Mechanical Property of W-TiC / Ti Composites via Chemical-Mechanical Milling Method, *Mater. Sci. Eng. A*, Elsevier B.V., 2024, **916**, p 147386, https://doi.org/10.1016/j.msea.2024.147386
23. Q. dong Qin, J. bo Qu, Y. e. Hu, Y. jiao Wu, and X. dong Su, Microstructural Characterization and Oxidation Resistance of Multi-component Equiatomic CoCrCuFeNi–TiO High-Entropy Alloy, *Int. J. Miner. Metall. Mater.*, 2018, **25**(11), p 1286–1293
24. N. Liu, M. Xu, Y.Y. Qian, and P.J. Zhou, Microstructure, Phase Stability, and Oxidation Resistance of (FeCoNi)$_{60}$Al$_{15}$Cr$_{25-x}$Ti$_x$ High-Entropy Alloys, *J. Alloys Compd.*, 2021, **870**(159320), p 7, https:/doi.org/https://doi.org/10.1016/j.jallcom.2021.159320
25. M. Laurent-Brocq, P.A. Goujon, J. Monnier, B. Villeroy, L. Perrière, R. Pirès and G. Garcin, Microstructure and Mechanical Properties of a CoCrFeMnNi High Entropy Alloy Processed by Milling and Spark Plasma Sintering, *J. Alloys Compd.*, 2019, **780**, p 856–865
26. Y. Xing, C.J. Li, Y.K. Mu, Y.D. Jia, K.K. Song, J. Tan, G. Wang, Z.Q. Zhang, J.H. Yi and J. Eckert, Journal of Materials Science & Technology Strengthening and Deformation Mechanism of High-Strength CrMnFeCoNi High Entropy Alloy Prepared by, *Powder Metall.*, 2023, **132**, p 119–131. https://doi.org/10.1016/j.jmst.2022.06.009
27. M.S. Mehranpour, H. Shahmir, A. Derakhshandeh and M. Nili-Ahmadabadi, Significance of Ti Addition on Precipitation in CoCrFeNiMn High-Entropy Alloy, *J. Alloys Compd.*, 2021, **888**, p 2–5
28. G. Qin, Z. Li, R. Chen, H. Zheng, C. Fan, L. Wang, Y. Su, H. Ding, J. Guo and H. Fu, CoCrFeMnNi High-Entropy Alloys Reinforced with Laves Phase by Adding Nb and Ti Elements, *J. Mater. Res.*, 2019, **34**(6), p 1011–1020
29. H. Shahmir, M.S. Mehranpour, A. Derakhshandeh, and M. Nili-Ahmadabadi, Microstructure Tailoring to Enhance Mechanical Properties in CoCrFeNiMn High-Entropy Alloy by Ti Addition and Thermomechanical Treatment, *Mater. Charact.*, Elsevier Inc., 2021, **182**, p 111513, https://doi.org/10.1016/j.matchar.2021.111513
30. S. Yamanaka, K. ichi Ikeda, and S. Miura, The Effect of Titanium and Silicon Addition on Phase Equilibrium and Mechanical Properties of CoCrFeMnNi-Based High Entropy Alloy, *J. Mater. Res.*, Springer International Publishing, 2021, **36**(10), p 2056–2070, https://doi.org/10.1557/s43578-021-00251-0
31. S.T. Shih and P.Y. Chen, Effects of Ti Addition on the Microstructure and Mechanical Properties of CoCrFeMnNi High-Entropy Alloy, *ISPACS 2021 - Int. Symp. Intell. Signal Process. Commun. Syst. 5G Dream to Reality, Proceeding*, IEEE, 2021, p 1–2
32. T.T. Shun, L.Y. Chang, and M.H. Shiu, Microstructure and Mechanical Properties of Multiprincipal Component CoCrFeNiMo$_x$ Alloys, *Mater. Charact.*, Elsevier Inc., 2012, **70**, p 63–67, https://doi.org/10.1016/j.matchar.2012.05.005
33. Ł Rogal, D. Kalita, A. Tarasek, P. Bobrowski, and F. Czerwinski, Effect of SiC Nano-Particles on Microstructure and Mechanical Properties of the CoCrFeMnNi High Entropy Alloy, *J. Alloys Compd.*, 2017, **708**, p 344–352. https://doi.org/10.1016/j.jallcom.2017.02.274
34. S. Singh, N. Wanderka, B.S. Murty, U. Glatzel, and J. Banhart, Decomposition in Multi-Component AlCoCrCuFeNi High-Entropy Alloy, *Acta Mater.*, Acta Materialia Inc., 2011, **59**(1), p 182–190, https://doi.org/10.1016/j.actamat.2010.09.023
35. P. Cui, Y. Ma, L. Zhang, M. Zhang, J. Fan, W. Dong, and P. Yu, Materials Science & Engineering A E Ff Ect of Ti on Microstructures and Mechanical Properties of High Entropy Alloys Based on CoFeMnNi System, *Mater. Sci. Eng. A*, Elsevier B.V., 2018, **737**, p 198–204, https://doi.org/10.1016/j.msea.2018.09.050
36. T.T. Shun, L.Y. Chang, and M.H. Shiu, Microstructures and Mechanical Properties of Multiprincipal Component CoCrFeNiTi$_x$ Alloys, *Mater. Sci. Eng. A*, Elsevier, 2012, **556**, p 170–174, https://doi.org/10.1016/j.msea.2012.06.075
37. M. Rahimian, N. Ehsani, N. Parvin, and H. reza Baharvandi, The Effect of Particle Size, Sintering Temperature and Sintering Time on the Properties of Al-Al2O3 Composites, Made by Powder Metallurgy, *J. Mater. Process. Technol.*, 2009, **209**(14), p 5387–5393, https://doi.org/10.1016/j.jmatprotec.2009.04.007
38. M. Çelebi, O. Güler, A.H. Karabacak, A. Çanakçı, S.B. Akçay, M. Kocaman, H. Çuvalcı, and T. Varol, Investigation of Microstructural, Hardness, and Wear Properties of AlCrCuFeNi High Entropy Alloys Produced by Hot-Pressing with the Enhancement of Manufacturability through Electroless Ag Incorporation, *Tribol. Int.*, Elsevier Ltd, 2025, **201**, p 110277, https://doi.org/10.1016/j.triboint.2024.110277
39. A. Sinha and Z. Farhat, Effect of Surface Porosity on Tribological Properties of Sintered Pure Al and Al 6061, *Mater. Sci. Appl.*, 2015, **06**(06), p 549–566. https://doi.org/10.4236/msa.2015.66059
40. M. Wang, Y. Wang, H. Liu, J. Wang, and F. Yan, Interrelated Effects of Temperature and Load on Fretting Behavior of SAF 2507 Super Duplex Stainless Steel, *Tribol. Int.*, Elsevier Ltd, 2019, **136**, p 140–147, https://doi.org/10.1016/j.triboint.2019.03.042
41. Y. Yu, B. Zhang, S. Zhu, Z. Zhang, W. Lu, T. Shen, and Z. Wang, Microstructural and Tribological Characteristics of In Situ Induced Chrome Carbide Strengthened CoCrFeMnNi High-Entropy Alloys, *J. Mater. Eng. Perform.*, Springer US, 2020, **29**(6), p 3714–3722, https://doi.org/10.1007/s11665-020-04872-0
42. C. Nagarjuna, A. Sharma, K. Lee, S.J. Hong, and B. Ahn, Microstructure, Mechanical and Tribological Properties of Oxide Dispersion Strengthened CoCrFeMnNi High-Entropy Alloys Fabricated by Powder Metallurgy, *J. Mater. Res. Technol.*, The Author(s), 2023, **22**, p 1708–1722, https://doi.org/10.1016/j.jmrt.2022.12.070
43. A. Erdogan, T. Yener and S. Zeytin, Fast Production of High Entropy Alloys (CoCrFeNiAl$_x$Ti$_y$) by Electric Current Activated Sintering System, *Vacuum, Elsevier*, 2018, **155**, p 64–72. https://doi.org/10.1016/j.vacuum.2018.05.027

44. S. Nam, M.J. Kim, J.Y. Hwang, and H. Choi, Strengthening of $Al_{0.15}CoCrCuFeNiTi_x$–C (x = 0, 1, 2) High-Entropy Alloys by Grain Refinement and Using Nanoscale Carbides via Powder Metallurgical Route, *J. Alloys Compd.*, 2018, **762**, p 29–37, https://doi.org/10.1016/j.jallcom.2018.05.180
45. K. Lentzaris, A. Poulia, E. Georgatis, A.G. Lekatou, and A.E. Karantzalis, Analysis of Microstructure and Sliding Wear Behavior of $Co_{1.5}CrFeNi_{1.5}Ti_{0.5}$ High-Entropy Alloy, *J. Mater. Eng. Perform.*, Springer US, 2018, **27**(10), p 5177–5186, https://doi.org/10.1007/s11665-018-3374-y
46. J. Joseph, N. Haghdadi, K. Shamlaye, P. Hodgson, M. Barnett, and D. Fabijanic, The Sliding Wear Behaviour of CoCrFeMnNi and $Al_xCoCrFeNi$ High Entropy Alloys at Elevated Temperatures, *Wear*, Elsevier B.V., 2019, **428**–**429**, p 32–44, https://doi.org/10.1016/j.wear.2019.03.002
47. Y. Wang, D. Li, J. Yang, J. Jin, M. Zhang, X. Wang, B. Li, Z. Hu, and P. Gong, Effect of Grain Size on the Tribological Behavior of CoCrFeMnNi High Entropy Alloy, *Materials (Basel).*, 2023, **16**(4), https://doi.org/10.3390/ma16041714
48. C. Nagarjuna, K. Yong, Y. Lee, S. Min, S. Ig, H. Seop, and S. Hong, Strengthening the Mechanical Properties and Wear Resistance of CoCrFeMnNi High Entropy Alloy Fabricated by Powder Metallurgy, *Adv. Powder Technol.*, Society of Powder Technology Japan, 2022, **33**(4), p 103519, https://doi.org/10.1016/j.apt.2022.103519
49. L. Liu, T. Han, S.C. Cao, Y. Liu, J. Shu, C. Zheng, T. Yu, Z. Dong, and Y. Liu, Enhanced Wearing Resistance of Carbide Reinforced FeCoNiCrMn High Entropy Alloy Prepared by Mechanical Alloying and Spark Plasma Sintering, *Mater. Today Commun.*, Elsevier Ltd, 2022, **30**, p 103127, https://doi.org/10.1016/j.mtcomm.2022.103127
50. A. Canakci, H. Cuvalci, T. Varol, F. Erdemir, S. Ozkaya and E.D. Yalcin, Microstructure and Abrasive Wear Behavior of $CuSn_{10}$–Graphite Composites Produced by Powder Metallurgy, *Powder Metall. Met. Ceram.*, 2014, **53**(5–6), p 275–287
51. P. Liu, W. Si, D. Zhang, S. Dai, B. Jiang, D. Shu, L. Wu, and C. Zhang, Microstructure and Friction Properties of $CoCrFeMnNiTi_x$ High-Entropy Alloy Coating by Laser Cladding, *Materials (Basel).*, 2022, **15**(13), p 4669
52. J. Wang, B. Zhang, Y. Yu, Z. Zhang, S. Zhu, and Z. Wang, Ti Content Effect on Microstructure and Mechanical Properties of Plasma-Cladded $CoCrFeMnNiTi_x$ High-Entropy Alloy Coatings, *Surf. Topogr. Metrol. Prop.*, 2020, **8**(015004), https://doi.org/10.1088/2051-672X/ab615b
53. L. Moravcikova-Gouvea, I. Moravcik, M. Omasta, J. Veselý, J. Cizek, P. Minárik, J. Cupera, A. Záděra, V. Jan, and I. Dlouhy, High-Strength $Al_{0.2}Co_{1.5}CrFeNi_{1.5}Ti$ High-Entropy Alloy Produced by Powder Metallurgy and Casting: A Comparison of Microstructures, Mechanical and Tribological Properties, *Mater. Charact.*, Elsevier, 2020, **159**, p 110046, https://doi.org/10.1016/j.matchar.2019.110046
54. H. Lee, A. Sharma, and B. Ahn, Dry Sliding Wear and Friction Behavior of Powder Metallurgy $FeCoNiAlSi_{0.2}$ High-Entropy Alloys, *Wear*, Elsevier B.V., 2023, **530**–**531**, p 205011, https://doi.org/10.1016/j.wear.2023.205011
55. R. Savinov and J. Shi, Microstructure, Mechanical Properties, and Corrosion Performance of Additively Manufactured CoCrFeMnNi High-Entropy Alloy before and after Heat Treatment, *Mater. Sci. Addit. Manuf.*, 2023, **2**(1), p 42
56. S. Öztürk, S. Önal, S.E. Sünbül, Ö. Şahin, K. İçin, and A. Furkan, Journal of Alloys and Compounds, *J. Alloys Compd.*, 2022, **903**(903), p 163867, https://doi.org/10.1016/j.jallcom.2022.163867
57. J. Ren, C. Mahajan, L. Liu, D. Follette, W. Chen, and S. Mukherjee, Corrosion Behavior of Selectively Laser Melted CoCrFeMnNi High Entropy Alloy, *Metals (Basel).*, 2019, **9**(10)
58. H. Peng, Z. Lin, R. Li, P. Niu and Z. Zhang, Corrosion Behavior of an Equiatomic CoCrFeMnNi High-Entropy Alloy- a Comparison Between Selective Laser Melting and Cast, *Front. Mater.*, 2020, **7**, p 1–11
59. X. Jin, X. Gu, F. Quan, X. Ran, K. Zhang and A. Mao, CoCrFeMnNi High-Entropy Alloy Powder with Excellent Corrosion Resistance and Soft Magnetic Property Prepared by Gas Atomization Method, *Materwiss. Werksttech.*, 2019, **50**(7), p 837–843
60. L. Qingqing, C. Xiaohong, W. Tian, H. Wang, P. Liu, H. Zhou, S. Fu, Y. Gao, M. Wan, and X. Wang, Comparison with 304 Stainless Steel in Simulated Body Fluids, *J. Alloys Compd.*, Elsevier, 2022, **897**, p 163036, https://doi.org/10.1016/j.jallcom.2021.163036
61. S.S. Liu, M. Zhang, G.L. Zhao, X.H. Wang and J.F. Wang, Microstructure and Properties of Ceramic Particle Reinforced FeCoNiCrMnTi High Entropy Alloy Laser Cladding Coating, *Intermetallics, Elsevier Ltd*, 2022, **140**, 107402. https://doi.org/10.1016/j.intermet.2021.107402
62. L. Jiang, Y. Lu, Y. Dong, T. Wang, Z. Cao, and T. Li, Annealing Effects on the Microstructure and Properties of Bulk High-Entropy $CoCrFeNiTi_{0.5}$ Alloy Casting Ingot, *Intermetallics*, Elsevier Ltd, 2014, **44**, p 37–43, https://doi.org/10.1016/j.intermet.2013.08.016
63. D. Choudhuri, T. Alam, T. Borkar, B. Gwalani, A.S. Mantri, S.G. Srinivasan, M.A. Gibson, and R. Banerjee, Formation of a Huesler-like L21 Phase in a CoCrCuFeNiAlTi High-Entropy Alloy, *Scr. Mater.*, Acta Materialia Inc., 2015, **100**, p 36–39, https://doi.org/10.1016/j.scriptamat.2014.12.006
64. X.F. Wang, Y. Zhang, Y. Qiao and G.L. Chen, Novel Microstructure and Properties of Multicomponent $CoCrCuFeNiTi_x$ Alloys, *Intermetallics*, 2007, **15**(3), p 357–362. https://doi.org/10.1016/j.intermet.2006.08.005
65. Y.J. Zhou, Y. Zhang, Y.L. Wang, and G.L. Chen, Solid Solution Alloys of AlCoCrFeNi Tix with Excellent Room-Temperature Mechanical Properties, *Appl. Phys. Lett.*, 2007, **90**(18), https://doi.org/10.1063/1.2734517
66. A.J. Pirlari, M. Emamy, A.A. Amadeh, and M. Naghizadeh, Elucidating the Effect of TiB2 Volume Percentage on the Mechanical Properties and Corrosion Behavior of Al5083-TiB_2 Composites, *J. Mater. Eng. Perform.*, Springer US, 2019, **28**(11), p 6912–6920, https://doi.org/10.1007/s11665-019-04403-6

Publisher's Note Springer Nature remains neutral with regard to jurisdictional claims in published maps and institutional affiliations.

Springer Nature or its licensor (e.g. a society or other partner) holds exclusive rights to this article under a publishing agreement with the author(s) or other rightsholder(s); author self-archiving of the accepted manuscript version of this article is solely governed by the terms of such publishing agreement and applicable law.